Auto-bifunctional Mechanism of Jagged Pt Nanowire for Hydrogen Evolution Kinetics via End-to-End Simulation

Geun Ho Gu¹, Juhyung Lim¹, Chengzhang Wan², Tao Cheng³, Heting Pu², Sungwon Kim¹, Juhwan Noh¹, Changhyeok Choi¹, Juhwan Kim¹, William A. Goddard, III⁴*, Xiangfeng Duan²*, Yousung Jung¹*

¹Department of Chemical and Biomolecular Engineering, Korea Advanced Institute of Science and Technology (KAIST), 291 Daehak-ro 34141, Daejeon 305-335, South Korea

²Department of Chemistry and Biochemistry, University of California, 607 Charles E. Young Drive East, Los Angeles, CA 90095-1569, USA.

³Institute of Functional Nano & Soft Materials, Soochow University Dushu-Lake Campus, Box 33, 199 Ren'ai Rd, Suzhou Industrial Park, Suzhou, Jiangsu, 215123, P.R. China

⁴Materials and Process Simulation Center, California Institute of Technology, 1200 E California Blvd, Pasadena CA 91125, USA.

Abstract

The extraordinary mass activity of Jagged Pt nanowires can substantially improve the economics of hydrogen evolution reaction (HER). However, it is a great challenge to fully unveil the HER kinetics driven by the jagged Pt nanowires with their multi-scale morphology. Herein we present an end-to-end framework that combines experiment, machine-learning, and multi-scale advances of the last decade to elucidate the HER kinetics catalyzed by jagged Pt nanowires in alkaline conditions. The bifunctional catalysis conventionally refers to the synergistic increase in activity by the combination of two different catalysts. We report that a mono-metal, such as jagged Pt nanowire, can exhibit bifunctional characteristics owing to its complex surface morphology where one site prefers electrochemical proton adsorption and another is responsible for activation, resulting in a four-fold increase in the activity. We find that the conventional design guideline that the sites with 0 eV Gibbs free energy of adsorption is optimal for HER does not hold in alkaline conditions, and rather, the energy between -0.2 and 0.0 eV is shown to be optimal. At reaction temperatures, the high activity arises from low coordination number (\leq 7) Pt atoms exposed by the jagged surface. Our current demonstration raises an emerging prospect to understand highly complex kinetic phenomena in nanoscale in full by implementing end-to-end multi-scale strategies.

Keywords

Machine learning, catalysts, kinetic Monte Carlo, hydrogen evolution reaction, multi-scale, Pt, jagged Pt nanowire

*Corresponding authors: wag@caltech.edu, xduan@chem.ucla.edu, or ysjn@kaist.ac.kr

Introduction

Deploying renewable hydrogen as fuel promises a low-carbon economy as it burns cleanly (no CO₂ production) to provide a source for nighttime electricity.¹ Yet, the current industrial production chain for hydrogen involves energy-intensive natural gas reforming. It is essential to develop economic, sustainable processes such as water-splitting electrolysis to steer the market towards the green energy future.² Presently, commercial electrolysis cells use Pt-based catalysts for hydrogen evolution reaction (HER) due to their high activity and stability,³ but the catalyst cost is a major bottleneck.⁴ One direction to lowering the fuel cell cost is to dramatically reduce the amount of Pt used while maintaining high activity through morphology control,^{5,6} along with other strategies such as the Pt alloys⁷ and interfacial interaction engineering.⁸ Here, **we focus on HER optimization via morphology control**.

Generally, three reactions are known to be involved in HER (see also the bottom left corner in Fig. 1):

- Volmer reaction (H⁺ + e⁻ + * \rightarrow H*, H₂O + e⁻ + * \rightarrow H* + OH⁻; * is a site),
- Heyrovsky reaction ($H^+ + e^- + H^* \rightarrow H_2 + *, H_2O + e^- + H^* \rightarrow H_2 + *+OH^-$), and
- Tafel reaction (H* + H* \rightarrow H₂ + 2*).

In acidic conditions, the Volmer reaction that proceeds via proton transfer from hydronium is accepted to be a fast reaction due to an abundance of protons in solution, while the Heyrovsky and Tafel reactions compete for H₂ formation. For alkaline conditions, which are technologically attractive due to the development of anion exchange membrane and nonprecious metal oxygen evolution reaction (OER) catalysts under alkaline conditions, the importance of HER increases. To understand the origin of the slow HER kinetics in alkaline conditions compared to acidic conditions, three recent theoretical studies focused on the pH-dependent HER kinetics for the Pt model surface. 12-14

Cheng et al. used Quantum Mechanics Molecular Dynamics to simulate the water/Pt(100) interface and demonstrated that the hydrogen binding strengthens with increasing pH as the Pt(100) repel water adsorption. Lamoureux et al. found that HER on Pt(111) proceeds via the Volmer-Heyrovsky pathway and the proton donor changes from hydronium to water with increasing pH. Intrinsically larger barrier for proton transfer from water in Helmholtz plane to the surface is the cause of slower HER kinetics in alkaline media. Liu et al. demonstrated similar conclusions but found that the HER proceeds through Volmer-Tafel.

Here, we report an end-to-end simulation of jagged Pt nanowire for HER in alkaline conditions using a machine learning multi-scale strategy¹⁵ with kinetic Monte Carlo (KMC) to reveal novel kinetic insights. This framework yields good agreement with the experimental measurements. We find that both Volmer and Tafel reactions are co-rate determining step (RDS), and notably, the monometallic jagged Pt nanowire offers a bifunctional mechanism: bridge sites more selective for Volmer, and top and hollow sites more selective for Tafel, with the two connected via fast diffusion of the adsorbed hydrogen atoms. The optimal hydrogen binding strength for HER is shown to be lower than zero (irrespective of site type), implying that the conventional design principle for HER to maximize the site activity with Gibbs free energy of adsorption of H being zero does not hold. The present analysis of surface kinetics reveals that top sites are the most active site for both Volmer and Tafel reaction, and those with low coordination numbers (≤7) are more active. These studies complement the recent report from Chen et al explaining the extremely high rate for the oxygen reduction reaction (ORR) on jagged Pt nanowires in terms of O* binding and H₂O binding on adjacent sites.¹¹6

Results and discussions

Simulation workflow and activity measurement of the jagged Pt nanowire. The kinetic simulation is performed using graph-theoretical KMC simulation.¹⁷ We model the alkaline HER system with Volmer, Heyrovsky, Tafel, and diffusion reactions. For the Volmer and Heyrovsky reactions, we considered proton transfer from H₂O (basic) as we perform simulation at pH of 14.14 The Supplementary Section 1 describes the derivation of reaction energy and activation energy using computational hydrogen electrode (CHE) and BEP relations built with the constant electrode potential (CEP) model. To obtain adsorption energy on the jagged Pt nanowire, we leverage the ReaxFF forcefield and effective medium theory (EMT)^{18,19} to synthesize jagged Pt nanowire (structure of which is in close agreement with the experimental chracterization^{5,16}) and generate the small jagged Pt slabs (see Supplementary Section 4) as a model surface of the jagged Pt nanowire. 5,16 We perform DFT calculations to compute the adsorption energy of 3413 binding sites of the slabs, local environment of which are extracted¹⁵ and converted to a labeled site representation to train machine learning model.²⁰ We test four models to predict Gibbs free energy of hydrogen adsorption, $\Delta_r G_{ads}$: Atom centered symmetric function (ACSF),²¹ crystal graph convolutional neural networks (CGCNN),²² Nearest atom distance-Gaussian process (NAD-GP; developed in this work)²³ and SchNet.²⁴ (see Supplementary Section 5). The best model is applied to the jagged Pt nanowire obtained using force field MD simulation.⁵ To account for lateral interaction, we develop and use the cluster expansion model derived from experiments as discussed in Supplementary Section 6 which sufficiently describe the H coverage on Pt surfaces.²⁵ We derive the energetics (see Supplementary Section 1) and apply BEP relations (see Supplementary Section 1 and 3) and perform KMC simulation to elucidate the mechanisms. The overall framework is illustrated in Fig. 1 and demonstrates that the emerging theoretical and machine learning methods enable the detailed simulation of complex large scale surfaces.

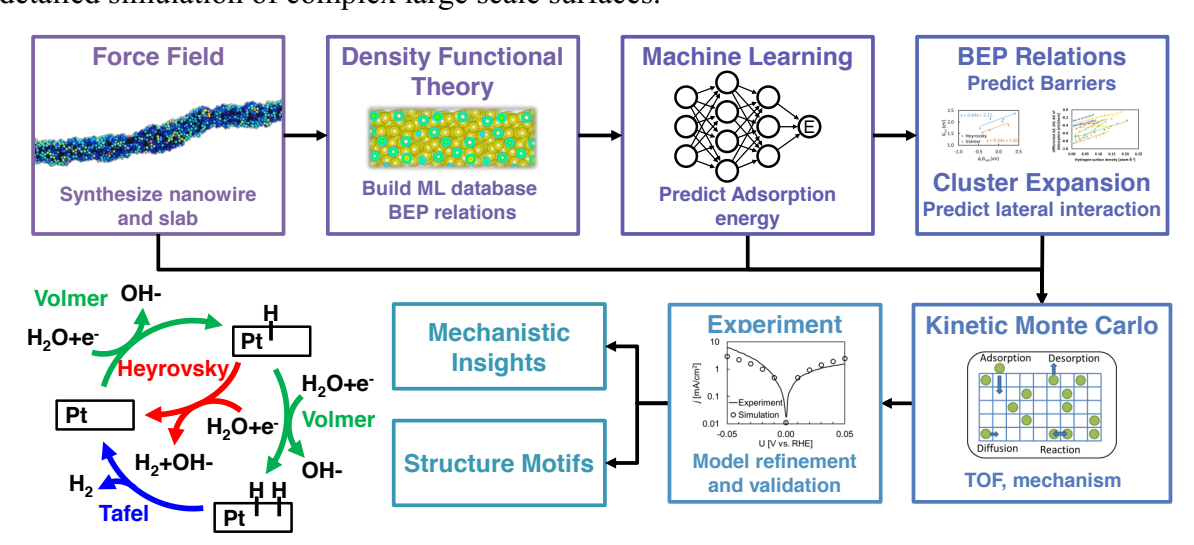


Fig. 1 | **End-to-end workflow for the jagged Pt nanowire simulation.** We combine the force field, density functional theory, machine learning, and kinetic modeling to perform multi-scale simulation of the alkaline HER of the jagged Pt nanowire. The model is validated by comparing the simulation result with experimental results, and the mechanism is analyzed. The graphic on the bottom left shows the alkaline HER mechanism involving Volmer, Heyrovsky, and Tafel reactions.

Validation of the model. Out of the four different machine learning models we tested for predicting $\Delta_r G_{ads}$, ACSF showed the lowest out of sample error (0.043 eV mean absolute error), thus, from here on, ACSF is used to predict $\Delta_r G_{ads}$ (see Fig. 2a and Supplementary Section 5). To quantitatively validate our kinetic simulation, we experimentally synthesized

jagged Pt nanowire using the method outlined in Ref^{5,6} and measured the exchange current density, symmetric factor, surface coverage, and Tafel slope (see Supplementary Section 8 for detail). To measure exchange current densities, i_0 , Butler-Volmer equation (-0.05 to 0.05 V vs. RHE), and micropolarization linear equation (-0.01 to 0.01 V vs. RHE) were fitted.²⁶ The KMC simulation and experiment are performed at room temperature, pH 14, and 1 bar of H_{2(g)}, and the results are compared in Fig. 2. To reproduce the experiment, Tafel barriers and Volmer barriers are adjusted by +0.06 eV and -0.097 eV (more details are discussed later). The simulated exchange current density (0.81, and 0.83 mA cm⁻² for Butler-Volmer and linear fitting, respectively) is in good agreement with the experimentally measured (0.87 and 0.70 mA cm⁻², respectively). The coverage (0.57 vs. 0.66 monolayers (ML) for simulation and experiment, respectively), and the Tafel slopes (72.9 vs. 73 mV/dec for simulation and experiment, respectively) are in close agreement as well. One discrepancy in the symmetric factor (0.45 vs. 0.13 for simulation and experiment, respectively) is due to the use of Pt(111) data of Ref⁹ (0.44) in the model. The use of a more realistic symmetric factor for the Volmer reaction averaged over different binding sites for the jagged nanowire would improve the model. We discuss the uncertainty of our model below.

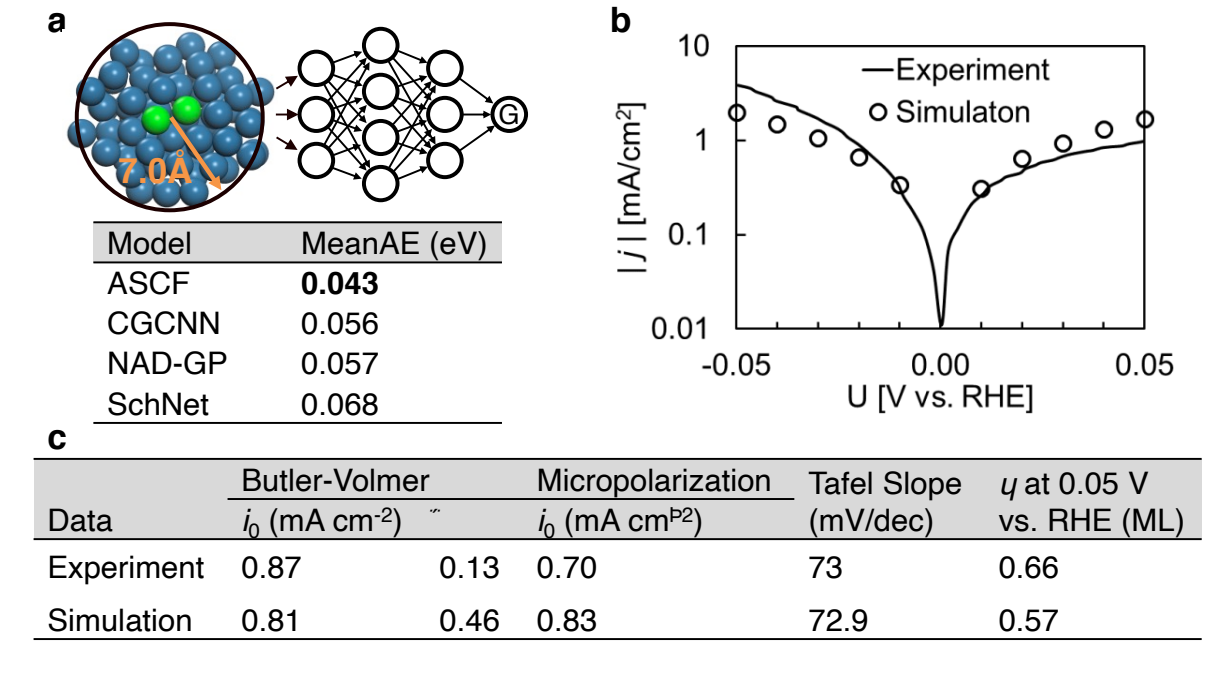


Fig. 2 | Validation of the machine learning and the kinetic Monte Carlo model, and comparison with the experiment. a $\Delta_r G_{ads}$ prediction machine learning architecture and the mean absolute error (MeanAE) for tested models. The local environment (< 7Å) of the binding site atoms (green color) is converted to labeled site representation,²⁰ and piped through machine learning models. We tested Atom centered symmetric function (ACSF),²¹ crystal graph convolutional neural networks (CGCNN),²² Nearest atom distance-Gaussian process (NAD-GP; developed in this work)²³ and SchNet,²⁴ and used ACSF for the rest of the article (see Supplementary Section 5 for detail). b-c The reaction is performed at room temperature with pH 14 and 1 bar of H_{2(g)} for (b) Tafel plot. The simulated exchange current density using Butler-Volmer and micropolaization, coverage (θ), and Tafel slope are shown in c and are in close agreement with the experiment. θ is the symmetric factor.

Hydrogen evolution reaction mechanism. The Gibbs free energy of hydrogen adsorption, $\Delta_{\rm r}G_{\rm ads}$, at the zero coverage limit follows the Gaussian shape as shown in Fig. 3a. Due to the lateral interaction, $\Delta_{\rm r}G_{\rm ads}$ shifts by 0.14 eV with the standard deviation of 0.08 eV. The Tafel and Volmer reactions are co-RDS as shown by the degree of rate control analysis²⁷ in Fig. 3b in agreement with the previous microkinetic model study on Pt(111).¹⁴ The Heyrovsky reaction is too slow to have any kinetic contribution, but the diffusion process of the adsorbed hydrogen

between various surface sites is very fast, at least 5 orders of magnitude faster than either the Tafel or Volmer reactions. Fig. 3c shows the average turnover frequency of Volmer and Tafel reaction vs. the time-averaged Gibbs free energy of adsorption, $\Delta_r G_{ads}$. In acidic condition, Volmer reaction (H transfer from H₃O⁺) is too fast to be RDS, ^{13,14} thus the binding site with $\Delta_{\rm r}G_{\rm ads}\cong 0$ would be the optimal as it is thermodynamically the most favorable for site occupancy probability and H₂ formation.²⁸ However, in basic condition, the center of the Volmer (H transfer from H₂O) and Tafel activity for our simulation is at $\Delta_r G_{ads} = -0.17$ eV and $\Delta_{\rm r}G_{\rm ads}=-0.10$ eV, respectively, as shown in Fig. 3c. If adsorption and associative desorption reactions are RDS, the optimal $\Delta_r G_{ads}$ is observed at which the two reactions have equal activity.²⁹ As Volmer reaction is faster for $\Delta_r G_{ads} < 0$, $\Delta_r G_{ads}$ lower than 0 eV is more optimal for the alkaline condition. This indicates that the design principle (e.g., $\Delta_r G_{ads}$ based screening) is not the same for the acidic and alkaline conditions. To understand the optimal $\Delta_{\rm r}G_{\rm ads}$, we simulate a single site Pt system using mean-field microkinetic model, and plot the $\Delta_{\rm r}G_{\rm ads}$ with the highest activity at 0 V vs. RHE, $\Delta_{\rm r}G_{\rm ads,opt}$, in Fig. 3d. The $\Delta_{\rm r}G_{\rm ads,opt}$ is -0.16 eV at pH 10 (where the alkaline Volmer is the adsorption RDS^{13,14}) and increases to -0.09 eV at pH 14.

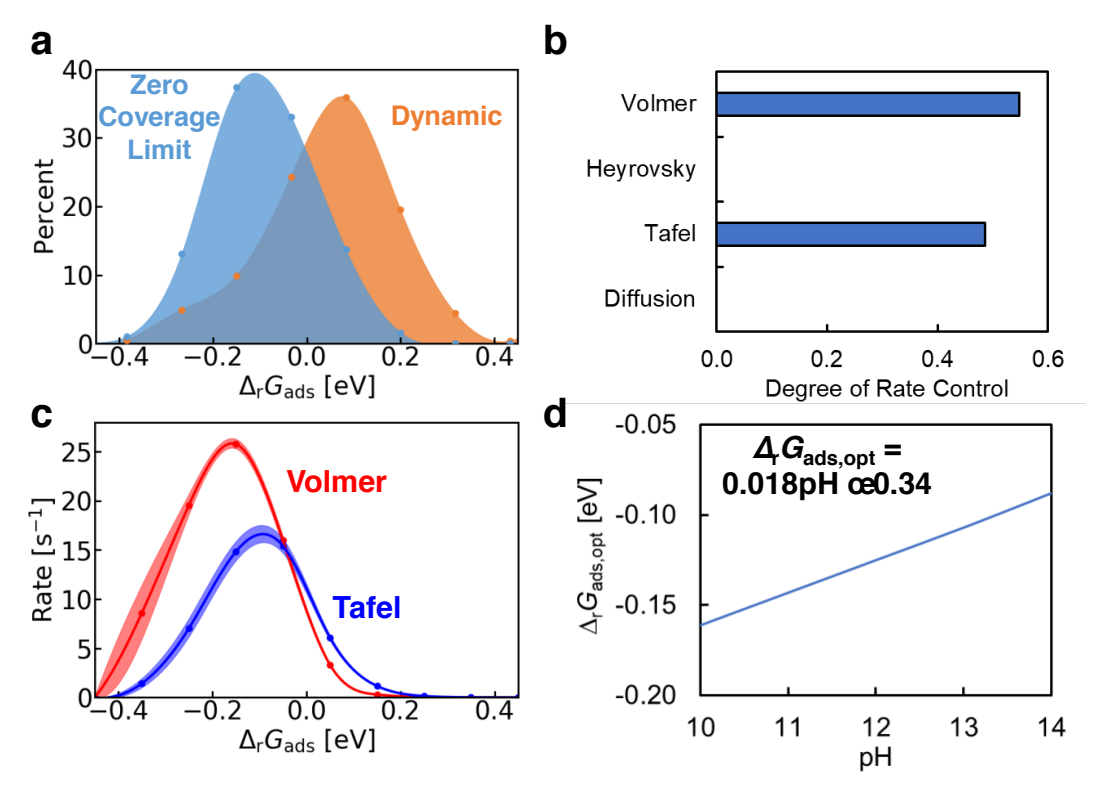


Fig. 3 | Analysis of kinetics on jagged Pt nanowire at 298K. a zero coverage limit vs. dynamic $\Delta_r G_{\text{ads}}$ calculated at pH 14 and -0.05 V vs. RHE. **b** the degree of rate control, $^{27} d \ln r_i / d (-G^{\circ}_{a,f,i}/RT)$ at pH 14 and -0.05 V vs. RHE. **c** averaged turnover frequency vs. $\Delta_r G_{\text{ads}}$ at -0.05 V vs. RHE where the shaded region indicates the 95% confidence interval and **d** the optimal Gibbs free energy of adsorption, $\Delta_r G_{\text{ads,opt}}$, vs. the pH at 0 V vs. RHE.

Auto-bifunctional mechanism of jagged Pt nanowire. The co-rate determining steps, the difference in the center of activity with respect to $\Delta_r G_{ads}$, and the wide $\Delta_r G_{ads}$ distribution indicates that the jagged Pt nanowire has a bifunctional mechanism. To demonstrate this, we analyzed the micro-spatial reaction network of the jagged Pt nanowire as shown in Fig. 4. The bifunctional catalyst uses a combination of two active sites to overcome two rate-determining steps to improve the overall activity. Conventionally, the two different catalysts are physically mixed or co-synthesized to create the bifunctional catalyst. Here, we find that a mono-metallic

catalyst can exhibit bifunctional characteristics via morphology. For a site with $\Delta_r G_{ads}$ of 0.0 eV, Volmer reaction is the RDS with the Gibbs free energy of activation (Fig. 4a), $G_{a,f}$, of 0.68 eV, while, for sites with $\Delta_r G_{ads}$ of -0.12 eV as an example, the Tafel reaction is the RDS with $G_{a,f}$, of 0.74 eV (Fig. 4b). On the jagged Pt nanowire, both of these sites co-exist on the surface, hence a monometallic auto-bifunctional mechanism is observed where proton electrochemically adsorb on one site (Volmer favored sites) and diffuse to a site with faster Tafel reaction to form hydrogen (Tafel favored sites).

Fig. 4d visualizes the difference in the Volmer and Tafel reaction rate and the diffusion between sites showing the bifunctional chemistry of the jagged Pt nanowire. The benefit of the bifunctionality can be measured by comparing the current density with and without hydrogen diffusion. We find that the activity increases by four-fold (461%) with hydrogen diffusion. To understand the bifunctional effect, we build a microkinetic model with two sites, $\Delta_r G_{ads}$ of which are different from each other. Fig. 5 shows the activity gain resulting from coupling the two sites, which demonstrates that the combination of a site with $\Delta_r G_{ads} > 0$ and a site with $\Delta_r G_{ads} < 0$ can lead to more than two orders of magnitude increase in activity. This bifunctional gain has been hypothethically predicted to occur in certain conditions, ³⁰ where we indeed confirm that the bifunctional gain occurs in the jagged Pt nanowire.

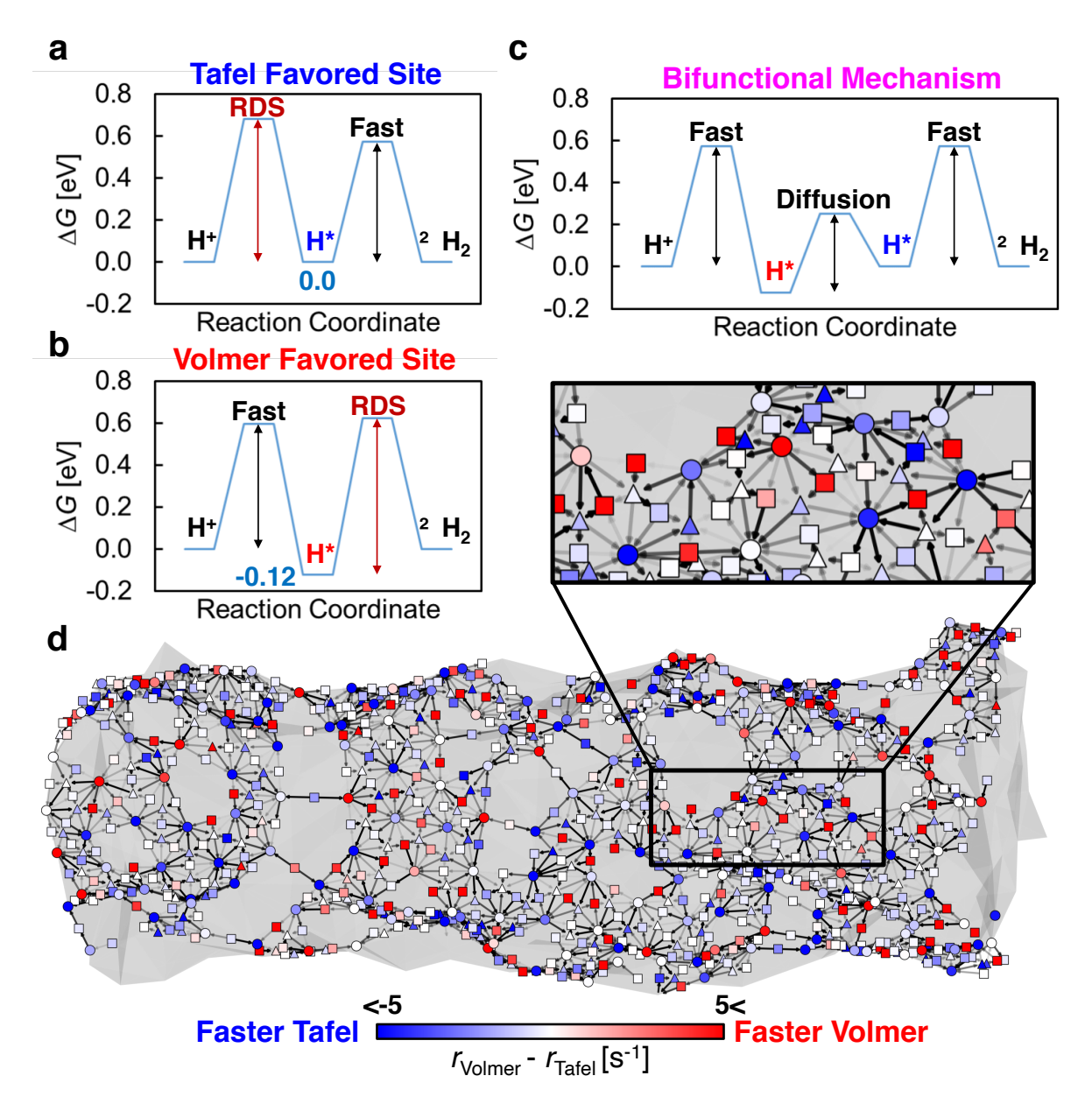


Fig. 4 | Bifunctional catalysis of the jagged Pt nanowire. a-b demonstrates the hydrogen evolution energetics for $\Delta_r G_{ads}$ of (a) 0.0 eV and (b) -0.12 eV. For a, and b, Volmer and Tafel reactions are rate-determining steps (RDS), respectively. The energetics in the top right corner of c demonstrates the bifunctional mechanism where the proton can electronically adsorb at Volmer favorable site and diffuse to Tafel favorable site to form $H_{2(g)}$. The nanowire visualization in d demonstrates the binding sites' reaction preference in colored symbols (Circle, square, and triangles are top, bridge, and hollow sites, respectively) where the blue and red color indicates a faster rate in Tafel, and Volmer reaction, respectively. We use the range between 5 and -5 as the standard deviation of the activity difference is ~5.11 s⁻¹. The arrows represent the direction of the net flux of hydrogen diffusion where darker black indicates larger net flux. The bifunctional mechanism accounts for a four-fold increase in activity. The reaction condition is pH 14, 298 K, and -0.05 V vs. RHE.

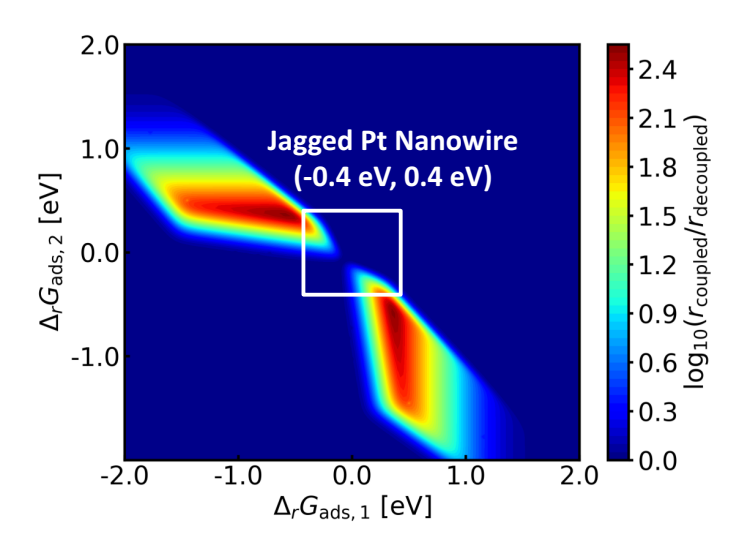


Fig. 5 | Bifunctional gain in activity with a combination of two sites. A two-site microkinetic model is built where $\Delta_r G_{\text{ads},1}$ and $\Delta_r G_{\text{ads},2}$ are the adsorption energy of the two sites. The color represents the bifunctional gain ratio where r_{coupled} and $r_{\text{decoupled}}$ are the ratio of HER rate when two sites are coupled and decoupled, respectively. More than two orders of magnitude gain in activity can be observed for the combination of two sites with negative and positive adsorption energy. The reaction condition is pH 14, 298K, and -0.05 V vs. RHE.

Volmer and Tafel activity by site type. We find that the activity is correlated to the binding site type. The activity of the Volmer and Tafel reaction is the highest for the top site as shown in Fig. 6a and c. The top sites behave as the active centers on the jagged Pt nanowire due to the favorable $\Delta_r G_{ads}$ distribution as shown in Fig. 6d and e. The difference between the site-averaged activity of the Volmer and Tafel reactions shows that Volmer reaction is faster for the bridge site and Tafel reaction is faster for the top and hollow site (Fig. 6b). Thus, the top sites consume all of the hydrogen atoms diffused from other top sites, and, as the Tafel reaction is faster, top sites also consume other hydrogen atoms diffused from the bridge sites.

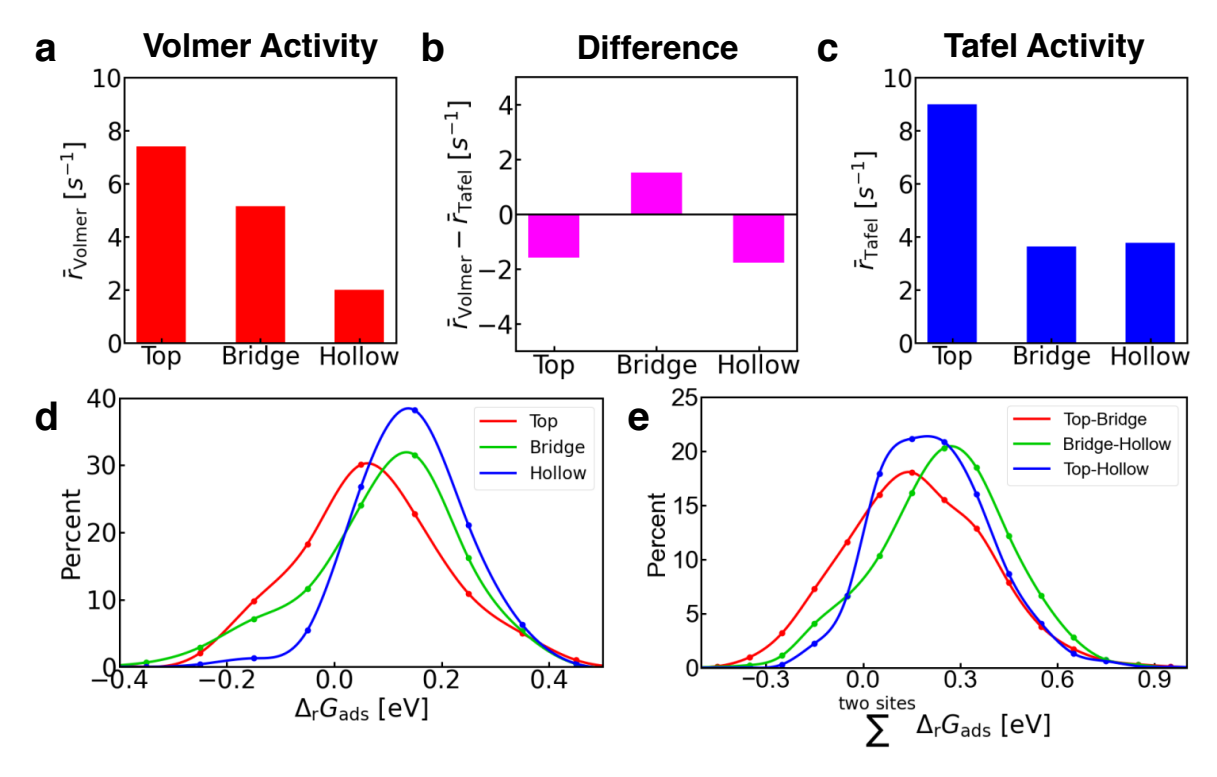


Fig. 6 | The HER activity of jagged Pt nanowire by the site. The average rate, \bar{r} , of Volmer (a), Tafel (c), and their difference (b) by sites. The distribution of $\Delta_r G_{ads}$ of sites (d) and the sums of $\Delta_r G_{ads}$ of two connected sites (e). The top sites are high in both Volmer and Tafel activity. The higher density of the top sites at $\Delta_r G_{ads} < 0.0$ eV results in higher Volmer activity. For Tafel activity, the optimum occurs at 0.0 eV as it optimizes the activation energy and the site occupation probability. The top sites have the highest Tafel activity as top-bridge and top-hollow pairs are dense near $\Delta_r G_{ads} = 0.0$ eV

Identification of active sites. We assess the correlation between activity and local binding site environment unsupervised using learning methods: smooth overlap of atomic positions kernel,³² (SOAP),31 average and t-stochastic neighbor embedding (t-SNE) dimensional reduction analysis.33 The SOAP and the kernel compute the similarity between sites' environment, and t-SNE reduces the binding site environments into two-dimensional space. Fig. 7a plots the two-dimensional representation of binding site environments with $\Delta_r G_{ads}$ as color. Not surprisingly we find that the $\Delta_r G_{ads}$ is correlated to the coordination number (CN) as shown in

Fig. S10.³⁴ We plot CN vs. $\Delta_r G_{ads}$ in Fig. 7b. For the top site, the correlation between CN and $\Delta_r G_{ads}$ is obvious, and the sites with CN \leq 7 are more optimal. Synthesizing the low coordinated Pt atoms can further improve the activity. The correlation between CN and $\Delta_r G_{ads}$ is weak for the bridge site and disappears for the hollow site. To identify structural motif besides CN, we manually compared structures of optimal and non-optimal sites, but no apparent trend could be found. Hence, the machine learning models can understand structural motifs beyond comprehensible motifs. Also, we plot the $\Delta_r G_{ads}$ and coordination number of top sites of the nanowire segment in Fig. 7c to demonstrate that exposed, low coordination sites are closer to the optimal $\Delta_r G_{ads}$.

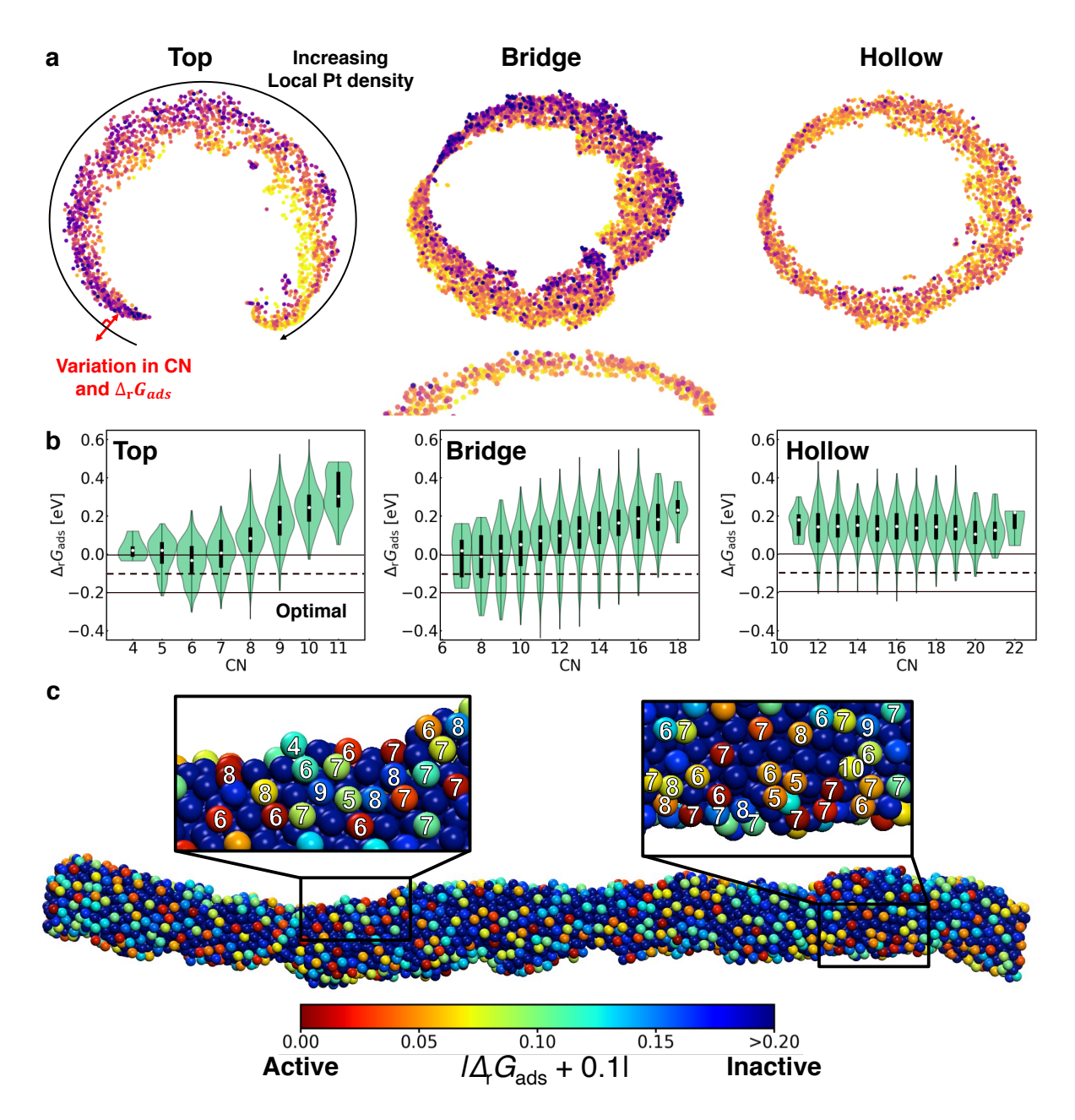


Fig. 7 | Visualization of the active binding sites. a Points and the distance between them represent the site and the dissimilarity between the sites visualized using SOAP descriptor,³¹ average kernel,³² and t-SNE dimensional reduction analysis.³³ The points are colored by sites' $\Delta_r G_{ads}$ for top, bridge, and hollow. As shown in Fig. S10, the structural unsupervised learning aligns the site environments based on the local Pt density (number of Pt atoms within 7 Å of the site) along the circular shape, while the direction orthogonal to the circle is correlated with the coordination number. The change in $\Delta_r G_{ads}$ (heat color) is more evident in the orthogonal direction, indicating that the $\Delta_r G_{ads}$ correlates with the coordination number. b Subsequently, the $\Delta_r G_{ads}$ is plotted against the coordination number. c A segment of Pt nanowire is visualized where the Pt atoms are colored by the distance from the optimal $\Delta_r G_{ads} \cong -0.1$ eV. The magnification shows that the Pt atoms with low coordination number have more optimal $\Delta_r G_{ads}$.

Limitations of the Model. Due to the multiscale nature of the phenomena and various associated methodologies used here, we address uncertainties of our results and discuss several limitations in this section. As mentioned previously, Tafel barriers and Volmer barriers are adjusted by a constant shift of +0.06 eV and -0.097 eV in constructing the BEP relation to reproduce the experimental current density as a function of applied potential. We note that the Tafel reaction BEP relations thus obtained fall within the data points constructed in Skúlason

et al⁹ for Pt(111), Pt(110), and Pt(100) (Fig. S7). These constant adjustments are similar to those of the microkinetic model developed on Pt(111)¹⁴ where Volmer barriers were adjusted by -0.07 eV and -0.03 eV for 0 ML and 0.83 ML, and Tafel barriers were adjusted by +0.05 eV for 0.83 ML. Also, the adjustment is within the standard deviation of Tafel and Volmer barriers calculated on Pt(111) using BEEF-ensemble³⁵ by Lamoureux et al (0.31 and 0.12 eV, respectively).¹³

We quantify the impact of the important parameters' uncertainty on the reproduced measurements and conclusions. In addition to Volmer and Tafel reactions (Fig. 3), the lateral interaction parameter is a sensitive parameter with a degree of rate control of 0.431. Thus, using the 95% confidence interval of Volmer barriers, Tafel barriers and lateral interaction parameter, the upper and lower bound of the Tafel slope, and exchange current density are calculated (Table S3). Overall, the experiment reproducibility is not significantly affected. The Tafel slope has the highest uncertainty from the Tafel barriers (71.1 to 85.7 mV/dec). While the Volmer reaction has the highest uncertainty in i_0 (0.36 to 1.72 mA cm⁻²), the i_0 is reproduced within an order of magnitude. The uncertainty in the bifunctional gain ratio is the largest with the Tafel barriers (278% to 612%; see Table S3). Overall, the bifunctional mechanism is consistently observed well within the uncertainty. We also assess the $\Delta_r G_{ads}$ distribution vs. CN within the uncertainty for the active site identification (Fig. S8). The lateral interaction parameter has the highest uncertainty in $\Delta_r G_{ads}$, but the lower coordinated Pt atoms remain as the active sites.

Our explicit/implicit hybrid DFT calculations have limitations in describing the Pt/water interface such as the pH-dependent interfacial water structure^{12,36,37} and cation effect.³⁸⁻⁴¹ The hydrogen binding strength correlates to the peaks in the underpotential deposition region and has shown to become stronger with increasing pH on Pt(100).³⁶ The quantum mechanics molecular dynamics study demonstrated that the enhanced binding on Pt(100) is due to the stronger electric potential used in alkaline conditions.¹² Also, the water structure becomes more rigid in strong electric field which may slow down the overall HER kinetics.³⁷ Cations form hydration shell in Helmholtz plane,^{38,39,41} and the HER activity and activation energy changes depending on the cation element.^{38,40} Quantifying these effects computationally for the jagged Pt nanowire is difficult due to the computational cost of the large scale explicit simulation, but some adjustments made to our model to reproduce the experimental current density may have contributed to implicitly and partially account for these fine effects.

Conclusions

We demonstrated the end-to-end framework to simulate the kinetics of jagged Pt nanowires with complex morphology using machine learning multiscale strategy, in good agreement with the experimental results in alkaline conditions. As Tafel and Volmer reactions are co-rate determining steps with distinct BEP relations, we find that the optimal $\Delta_r G_{ads}$ for the overall rate in alkaline conditions is lower than that in the acidic condition ($\Delta_r G_{ads} < 0$). Owing to the co-rate determining step and the wide distribution of $\Delta_r G_{ads}$, the jagged Pt nanowire shows the auto-bifunctional mechanism where the stronger binding sites adsorb proton and weaker binding site activates hydrogen. The top sites are the most active for both Volmer and Tafel reactions, but, as the Tafel reaction is faster, top sites also consume hydrogen diffused from bridge sites. Unsupervised-learning demonstrates that $\Delta_r G_{ads}$ is correlated to the coordination number, and we find that sites with $CN \le 7$ are associated with high activity. Beyond the single metal catalyst, we believe that the demonstrated end-to-end simulation framework has the potential to elucidate the synergistic mechanisms of multi-component alloys and metal-support catalysts, and aid in the design of effective catalysts.

Methods

Energetics. To compute the Gibbs free energy of reaction, $\Delta_r G$, and activation, $G_{a,f}$, we use the computational hydrogen electrode (CHE). $\Delta_r G$ for the four reactions are

Volmer:
$$\Delta_{\rm r}G = \Delta_{\rm r}G_{{\rm ads},i} + {\rm e}U_{\rm SHE} + {\rm ln}\ 10\ k_BT{\rm pH}$$

Heyrovsky: $\Delta_{\rm r}G = -\Delta_{\rm r}G_{{\rm ads},i} + eU_{\rm SHE} + {\rm ln}\ 10\ k_BT{\rm pH}$
Tafel: $\Delta_{\rm r}G = -\Delta_{\rm r}G_{{\rm ads},i} - \Delta_{\rm r}G_{{\rm ads},j}$
Diffusion: $\Delta_{\rm r}G = \Delta_{\rm r}G_{{\rm ads},i} - \Delta_{\rm r}G_{{\rm ads},j}$

where $\Delta_r G_{\mathrm{ads},i}$ is the Gibbs free energy of H_2 adsorption for site i, U_{SHE} is electrode potential referenced from the standard hydrogen electrode, k_{B} is the Boltzman constant, and T is the temperature. For Tafel reaction, i and j indiciates the two site undergoing the hydrogen coupling, and, for diffusion reaction, hydrogen is diffusing from site j to i. $G_{\mathrm{a,f}}$ are computed by

Volmer:
$$G_{a,f} = \alpha(\Delta_r G_{ads,i}) + (1 - \beta)eU_{SHE} + G^{\circ}_{a,f}$$

Heyrovsky: $G_{a,f} = \alpha(-\Delta_r G_{ads,i}) + (1 - \beta)eU_{SHE} + G^{\circ}_{a,f}$
Tafel: $G_{a,f} = \alpha\Delta_r G_{ads}(-\Delta_r G_{ads,i} - \Delta_r G_{ads,j}) + (1 - \beta)eU_{SHE} + G^{\circ}_{a,f}$
Diffusion: $G_{a,f} = 0.435\Delta_r G_{ads,i} - 0.565\Delta_r G_{ads,j} + 0.184$

where α is the slope of for the dependence of $G_{a,f}$ on coverage, β is the symmetric factor, $G_{a,f}^{\circ}$ is the $G_{a,f}$ at $\Delta_r G_{ads} = U_{SHE} = pH = 0$. We used the parameters from the literature if available. Otherwise, we used DFT with CEP method⁴² to parameterize them. The derivation of these equations, the source of parameters, and the computation of the constants are discussed in Supplementary Section 1. The DFT calculation details and the DFT calculation of missing parameters are discussed in Supplementary sections 2 and 3, respectively.

Adsorption energy calculation using machine learning. We compute the adsorption energy of hydrogen using a machine learning model. To train our model, we used DFT to compute 3413 adsorption energies of various sites on jagged Pt slabs made using ReaxFF (see Supplementary Section 4). We used atom centered symmetric function²¹ to compute binding energy as it performed the best out of several models we tested. We used the labeled site representation and ensemble method discussed in our previous work.²⁰ To identify binding sites on jagged Pt nanowire, we used the alpha shape algorithm which yields surface area close to those obtained with the cyclic voltammetry curve.^{5,20} The details of the alpha shape algorithm, model cross-validation, and implementation are discussed in Supplementary Section 5.

Coverage effect. We derived a cluster expansion model to calculate differential adsorption energy with respect to the coverage from 11 experimental data of Pt(111), Pt(100), and Pt(100). We find that the change in differential adsorption energy is fairly constant with respect to the spatial hydrogen surface density. We exploit this to increase the energy of the system during

KMC simulation by 0.098 eV, for every pair of hydrogen within 2.78 Å. The details of the derivation are discussed in Supplementary Section 6.

Kinetic Monte Carlo simulation. We implement the graph-theoretical kinetic Monte Carlo algorithm as outlined in Stamatakis et al, 17 and implemented the reaction constant scaling presented by Núñez et al 43 to speed up the simulation. The detailed pseudo-code is provided in Supplementary Section 7. The Volmer and Tafel rate of a site i is calculated by

$$r_{\text{Volmer},i} = \frac{N_{\text{Volmer},i}}{t}$$

$$r_{\text{Tafel},i} = \frac{1}{t} \sum_{i} \frac{N_{\text{Tafel},i,j}}{2}$$
(3)

where t is the total KMC simulation time, $N_{\text{Volmer},i}$ is the number of Volmer reaction occurred involving site i, $N_{\text{Tafel},i,j}$ is the number of Tafel reaction occurred from the site i and j.

Experiment. The experimental detail is discussed in Supplementary Section 8.

Data availability

All data used to generate the results in this paper is found at https://github.com/kaist-amsg. The repository includes the binding energy data for training machine learning models and the structures of CEP DFT calculations.

Competing interests

The authors declare no competing interests.

Additional information

Supplementary information is available for this paper at .

Correspondence and requests for materials should be addressed to Y.J., X. D, or W.A.G..

Acknowledgments

G. G. is grateful to Dr. Marcel P. Núñez for the useful discussion of the kinetic Monte Carlo simulation. Y.J. acknowledges the financial support from the National Research Foundation of Korea (NRF-2017R1A2B3010176). T. C. acknowledges the financial support from the National Natural Science Foundation of China (Grant No. 2190030094) and the Natural Science Foundation of Jiangsu Province (Grant No. SBK20190810).

References

- (1) Stringer, J.; Horton, L.; Singer, M.; Ahearne, J.; Crabtree, G.; Baker, C.; DeJonghe, L.; Herbst, J.; Dresselhaus, M.; Smalley, R.; Stoller, R. *Basic Research Needs To Assure A Secure Energy Future: A Report from the Basic Energy Science Advisory Committee*, U.S.A., 2003.
- (2) Miller, E.; Ainscough, C.; Talapatra, A.; Record, D. o. E. H. a. F. C. P., Ed. 2014.
- (3) Vesborg, P. C. K.; Seger, B.; Chorkendorff, I. Recent Development in Hydrogen Evolution Reaction Catalysts and Their Practical Implementation. *J. Phys. Chem. Lett.* **2015**, *6*, 951.
- (4) Schmidt, O.; Gambhir, A.; Staffell, I.; Hawkes, A.; Nelson, J.; Few, S. Future cost and performance of water electrolysis: An expert elicitation study. *Int. J. Hydrog. Energy* **2017**, *42*, 30470.
- (5) Li, M.; Zhao, Z.; Cheng, T.; Fortunelli, A.; Chen, C.-Y.; Yu, R.; Zhang, Q.; Gu, L.; Merinov, B. V.; Lin, Z.; Zhu, E.; Yu, T.; Jia, Q.; Guo, J.; Zhang, L.; Goddard, W. A.; Huang, Y.; Duan, X.

- Ultrafine jagged platinum nanowires enable ultrahigh mass activity for the oxygen reduction reaction. *Science* **2016**, *354*, 1414.
- (6) Li, M.; Duanmu, K.; Wan, C.; Cheng, T.; Zhang, L.; Dai, S.; Chen, W.; Zhao, Z.; Li, P.; Fei, H.; Zhu, Y.; Yu, R.; Luo, J.; Zang, K.; Lin, Z.; Ding, M.; Huang, J.; Sun, H.; Guo, J.; Pan, X.; Goddard, W. A.; Sautet, P.; Huang, Y.; Duan, X. Single-atom tailoring of platinum nanocatalysts for high-performance multifunctional electrocatalysis. *Nat. Catal.* **2019**, *2*, 495.
- (7) Greeley, J.; Jaramillo, T. F.; Bonde, J.; Chorkendorff, I.; Nørskov, J. K. Computational high-throughput screening of electrocatalytic materials for hydrogen evolution. *Nat. Mater.* **2006**, *5*, 909.
- (8) Dubouis, N.; Grimaud, A. The hydrogen evolution reaction: from material to interfacial descriptors. *Chem. Sci.* **2019**, *10*, 9165.
- (9) Skúlason, E.; Tripkovic, V.; Björketun, M. E.; Gudmundsdóttir, S.; Karlberg, G.; Rossmeisl, J.; Bligaard, T.; Jónsson, H.; Nørskov, J. K. Modeling the Electrochemical Hydrogen Oxidation and Evolution Reactions on the Basis of Density Functional Theory Calculations. *J. Phys. Chem. C* **2010**, *114*, 18182.
- (10) Fang, Y.-H.; Wei, G.-F.; Liu, Z.-P. Catalytic Role of Minority Species and Minority Sites for Electrochemical Hydrogen Evolution on Metals: Surface Charging, Coverage, and Tafel Kinetics. *J. Phys. Chem. C* **2013**, *117*, 7669.
- (11) Zheng, Y.; Jiao, Y.; Vasileff, A.; Qiao, S.-Z. The Hydrogen Evolution Reaction in Alkaline Solution: From Theory, Single Crystal Models, to Practical Electrocatalysts. *Angew. Chem. Int. Ed.* **2018**, *57*, 7568.
- (12) Cheng, T.; Wang, L.; Merinov, B. V.; Goddard, W. A. Explanation of Dramatic pH-Dependence of Hydrogen Binding on Noble Metal Electrode: Greatly Weakened Water Adsorption at High pH. *J. Am. Chem. Soc.* **2018**, *140*, 7787.
- (13) Lamoureux, P. S.; Singh, A. R.; Chan, K. pH Effects on Hydrogen Evolution and Oxidation over Pt(111): Insights from First-Principles. *ACS Catal.* **2019**, *9*, 6194.
- (14) Liu, L.; Liu, Y.; Liu, C. Enhancing the Understanding of Hydrogen Evolution and Oxidation Reactions on Pt(111) through Ab Initio Simulation of Electrode/Electrolyte Kinetics. *J. Am. Chem. Soc.* **2020**, *142*, 4985.
- (15) Chen, Y.; Huang, Y.; Cheng, T.; Goddard, W. A. Identifying Active Sites for CO2 Reduction on Dealloyed Gold Surfaces by Combining Machine Learning with Multiscale Simulations. *J. Am. Chem. Soc.* **2019**, *141*, 11651.
- (16) Chen, Y.; Cheng, T.; Goddard Iii, W. A. Atomistic Explanation of the Dramatically Improved Oxygen Reduction Reaction of Jagged Platinum Nanowires, 50 Times Better than Pt. *J. Am. Chem. Soc.* **2020**, *142*, 8625.
- (17) Stamatakis, M.; Vlachos, D. G. A graph-theoretical kinetic Monte Carlo framework for onlattice chemical kinetics. *J. Chem. Phys.* **2011**, *134*, 214115.
- (18) Jacobsen, K. W.; Stoltze, P.; Nørskov, J. K. A semi-empirical effective medium theory for metals and alloys. *Surf Sci.* **1996**, *366*, 394.
- (19) Senftle, T. P.; Hong, S.; Islam, M. M.; Kylasa, S. B.; Zheng, Y.; Shin, Y. K.; Junkermeier, C.; Engel-Herbert, R.; Janik, M. J.; Aktulga, H. M.; Verstraelen, T.; Grama, A.; van Duin, A. C. T. The ReaxFF reactive force-field: development, applications and future directions. *Npj Comput. Mater.* **2016**, *2*, 15011.
- (20) Gu, G. H.; Noh, J.; Kim, S.; Back, S.; Ulissi, Z. W.; Jung, Y. Practical Deep-Learning Representation for Fast Heterogeneous Catalyst Screening. *J. Phys. Chem. Lett.* **2020**, Accepted.
- (21) Behler, J. Atom-centered symmetry functions for constructing high-dimensional neural network potentials. *J. Chem. Phys.* **2011**, *134*, 074106.

- (22) Xie, T.; Grossman, J. C. Crystal Graph Convolutional Neural Networks for an Accurate and Interpretable Prediction of Material Properties. *Phys. Rev. Lett.* **2018**, *120*, 145301.
- (23) Rasmussen, C. E. In *Advanced Lectures on Machine Learning: ML Summer Schools 2003, Canberra, Australia, February 2 14, 2003, Tübingen, Germany, August 4 16, 2003, Revised Lectures*; Bousquet, O., von Luxburg, U., Rätsch, G., Eds.; Springer Berlin Heidelberg: Berlin, Heidelberg, 2004, p 63.
- (24) Schütt, K. T.; Sauceda, H. E.; Kindermans, P. J.; Tkatchenko, A.; Müller, K. R. SchNet A deep learning architecture for molecules and materials. *J. Chem. Phys.* **2018**, *148*, 241722.
- (25) Karlberg, G. S.; Jaramillo, T. F.; Skúlason, E.; Rossmeisl, J.; Bligaard, T.; Nørskov, J. K. Cyclic Voltammograms for H on Pt(111) and Pt(100) from First Principles. *Phys. Rev. Lett.* **2007**, *99*, 126101.
- (26) Lu, S.; Zhuang, Z. Investigating the Influences of the Adsorbed Species on Catalytic Activity for Hydrogen Oxidation Reaction in Alkaline Electrolyte. *J. Am. Chem. Soc.* **2017**, *139*, 5156.
- (27) Campbell, C. T. The Degree of Rate Control: A Powerful Tool for Catalysis Research. *ACS Catal.* **2017**, *7*, 2770.
- (28) Nørskov, J. K.; Bligaard, T.; Logadottir, A.; Kitchin, J. R.; Chen, J. G.; Pandelov, S.; Stimming, U. Trends in the Exchange Current for Hydrogen Evolution. *J. Electrochem. Soc.* **2005**, *152*, J23.
- (29) Andersen, M.; Medford, A. J.; Nørskov, J. K.; Reuter, K. Scaling-Relation-Based Analysis of Bifunctional Catalysis: The Case for Homogeneous Bimetallic Alloys. *ACS Catal.* **2017**, *7*, 3960.
- (30) Andersen, M.; Medford, A. J.; Nørskov, J. K.; Reuter, K. Analyzing the Case for Bifunctional Catalysis. *Angew. Chem. Int. Ed.* **2016**, *55*, 5210.
- (31) Bartók, A. P.; Kondor, R.; Csányi, G. On representing chemical environments. *Phys. Rev. B* **2013**, *87*, 184115.
- (32) Himanen, L.; Jäger, M. O. J.; Morooka, E. V.; Federici Canova, F.; Ranawat, Y. S.; Gao, D. Z.; Rinke, P.; Foster, A. S. DScribe: Library of descriptors for machine learning in materials science. *Comput. Phys. Commun.* **2020**, *247*, 106949.
- (33) van der Maaten, L.; Hinton, G. Visualizing Data using t-SNE. *Journal of Machine Learning Research* **2008**, *9*, 2579.
- (34) Calle-Vallejo, F.; Loffreda, D.; Koper, M. T. M.; Sautet, P. Introducing structural sensitivity into adsorption—energy scaling relations by means of coordination numbers. *Nat. Chem* **2015**, *7*, 403.
- (35) Studt, F.; Abild-Pedersen, F.; Varley, J. B.; Nørskov, J. K. CO and CO2 Hydrogenation to Methanol Calculated Using the BEEF-vdW Functional. *Catal. Lett.* **2013**, *143*, 71.
- (36) Sheng, W.; Zhuang, Z.; Gao, M.; Zheng, J.; Chen, J. G.; Yan, Y. Correlating hydrogen oxidation and evolution activity on platinum at different pH with measured hydrogen binding energy. *Nat. Commun.* **2015**, *6*, 5848.
- (37) Ledezma-Yanez, I.; Wallace, W. D. Z.; Sebastián-Pascual, P.; Climent, V.; Feliu, J. M.; Koper, M. T. M. Interfacial water reorganization as a pH-dependent descriptor of the hydrogen evolution rate on platinum electrodes. *Nature Energy* **2017**, *2*, 17031.
- (38) Liu, E.; Li, J.; Jiao, L.; Doan, H. T. T.; Liu, Z.; Zhao, Z.; Huang, Y.; Abraham, K. M.; Mukerjee, S.; Jia, Q. Unifying the Hydrogen Evolution and Oxidation Reactions Kinetics in Base by Identifying the Catalytic Roles of Hydroxyl-Water-Cation Adducts. *J. Am. Chem. Soc.* **2019**, *141*, 3232.
- (39) Jiao, L.; Liu, E.; Mukerjee, S.; Jia, Q. In Situ Identification of Non-Specific Adsorption of Alkali Metal Cations on Pt Surfaces and Their Catalytic Roles in Alkaline Solutions. *ACS Catal.* **2020**, *10*, 11099.
- (40) Weber, D. J.; Janssen, M.; Oezaslan, M. Effect of Monovalent Cations on the HOR/HER Activity for Pt in Alkaline Environment. *J. Electrochem. Soc.* **2019**, *166*, F66.

- (41) Strmcnik, D.; Kodama, K.; van der Vliet, D.; Greeley, J.; Stamenkovic, V. R.; Marković, N. M. The role of non-covalent interactions in electrocatalytic fuel-cell reactions on platinum. *Nat. Chem* **2009**, *1*, 466.
- (42) Van den Bossche, M.; Skúlason, E.; Rose-Petruck, C.; Jónsson, H. Assessment of Constant-Potential Implicit Solvation Calculations of Electrochemical Energy Barriers for H2 Evolution on Pt. *J. Phys. Chem. C* **2019**, *123*, 4116.
- (43) Núñez, M.; Robie, T.; Vlachos, D. G. Acceleration and sensitivity analysis of lattice kinetic Monte Carlo simulations using parallel processing and rate constant rescaling. *J. Chem. Phys.* **2017**, *147*, 164103.

Supporting Information

Auto-bifunctional Mechanism of Jagged Pt Nanowire for Hydrogen Evolution Kinetics via End-to-End Simulation

Geun Ho Gu¹, Juhyung Lim¹, Chengzhang Wan², Tao Cheng³, Heting Pu². Sungwon Kim¹, Juhwan Noh¹, Changhyeok Choi¹, Juhwan Kim¹, William A. Goddard, III⁴*, Xiangfeng Duan²*, Yousung Jung¹*

¹Department of Chemical and Biomolecular Engineering, Korea Advanced Institute of Science and Technology (KAIST), 291 Daehak-ro 34141, Daejeon 305-335, South Korea

²Department of Chemistry and Biochemistry, University of California, 607 Charles E. Young Drive East, Los Angeles, CA 90095-1569, USA.

³Institute of Functional Nano & Soft Materials, Soochow University Dushu-Lake Campus, Box 33, 199 Ren'ai Rd, Suzhou Industrial Park, Suzhou, Jiangsu, 215123, P.R. China

⁴Materials and Process Simulation Center, California Institute of Technology, 1200 E California Blvd, Pasadena CA 91125, USA.

Contents

1. Gibbs free energy of reaction and activation.	S2
1.1. Computational hydrogen electrode	S2
1.2. Gibbs free energy of reaction	S3
1.3. Gibbs free energy of activation	S4
2. Density functional theory calculation details	S8
3. Brønsted-Evans-Polanyi (BEP) relation development	S9
4. ReaxFF MD Simulation of the jagged Pt nanowire	S9
5. Gibbs free energy of adsorption prediction via machine learning model development	S11
5.1. The Gibbs free energy of adsorption database	S11
5.2. Data Preprocessing	S11
5.3. Model training and validation	S12
5.4. Application to Pt Surface	S13
6. Coverage effect model development	S14
7. Graphic theoretical kinetic Monte Carlo simulation	S16
7.1. Pt surface graph generation, and reaction graph definition	S17
7.2. Kinetic Monte Carlo algorithm	S18
7.3. Model validation, degree of rate control analysis, uncertainty, and adjustments	S18
7.4. Effect of jagged Pt nanowire length	S19
8. Experimental details	S22
8.1. Synthesis of PtNi alloy nanowire on carbon	S22
8.2. Electrochemical dealloying of PtNi nanowire to synthesize jagged Pt nanowire	S22
8.3. Electrochemical hydrogen evolution/oxidation reaction test	S22
8.4. Obtaining exchange current density, symmetric factor, and Tafel slope from the HER/HOR Polariza	
9. Supplementary Figures and Tables	S24
10. Reference	

1. Gibbs free energy of reaction and activation

Our model for Gibbs free energy of reaction ($\Delta_r G$) and activation (G_a) for the electrochemical reaction of a proton on the surface depends on three factors: (1) pH, (2) electrode potential and (3) coverage. Here, we summarize the derivation of $\Delta_r G$ and G_a which is an extension of Ref.^{1,2} Though we only simulate alkaline chemistry (proton transfer from H₂O), we summarize derivation for acidic conditions (proton transfer from H₃O⁺) as well.

1.1. Computational hydrogen electrode

The computational hydrogen electrode (CHE) pioneered by Nørskov and coworkers provides a convenient way to account for the electrode potential for electrochemical reactions.³ The key for this method is to treat the electrochemical reaction as the removal/addition of a proton and an electron and the usage of the standard hydrogen electrode (SHE) as the reference electrode. For SHE reference electrode, the electrode potential is zero when

$$H_{(aq)}^{+} + e^{-} \rightarrow \frac{1}{2} H_{2(g)}$$
 (4)

is in equilibrium at the $H_{2(g)}$ pressure of 1 bar and pH of 0. Thus, the sum of chemical potentials at each side of the reaction is equal.

$$\mu^{\circ}_{\mathrm{H}_{(\mathrm{aq})}^{+}} + \mu^{0V}_{\mathrm{e}} = \frac{1}{2} \mu^{\circ}_{\mathrm{H}_{2(\mathrm{g})}} \tag{5}$$

where $\mu_i^{U_{\text{SHE}}}$ indicates the chemical potential of species i at the SHE referenced potential of U_{SHE} . To compute the chemical potential of proton and electron, the equation is rearranged and $\mu_{\text{e}^-}^{U_{\text{SHE}}}$ is added to both side of the equation:

$$\mu^{\circ}_{H_{(aq)}^{+}} + \mu^{U_{SHE}}_{e^{-}} = \frac{1}{2}\mu^{\circ}_{H_{2(g)}} - eU_{SHE}, \qquad eU_{SHE} = \mu^{0V}_{e^{-}} - \mu^{U_{SHE}}_{e^{-}}$$
(6)

To account for the change in the chemical potential due to the pH, $\mu^{\circ}_{H_{(aq)}^{+}} = \mu_{H_{(aq)}^{+}} - \ln 10 \ k_{B}T$ pH is substituted:

$$\mu_{\rm H_{(aq)}^+} + \mu_{\rm e^-}^{U_{\rm SHE}} = \frac{1}{2} \mu^{\circ}_{\rm H_{2(g)}} - eU_{\rm SHE} - \ln 10 \ k_{\rm B}T{\rm pH}$$
 (7)

The equation (7) can be conveniently used to calculate the energetics for electrochemical reactions involving proton and electrons using DFT as it only requires the DFT calculation of hydrogen gas.

1.2. Gibbs free energy of reaction

The Volmer reaction, $H_{(aq)}^+ + e^- + * \rightarrow H^*$, is the electrochemical adsorption of proton where * indicates the binding site. The $\Delta_r G$ of this reaction is

$$\Delta_{\rm r}G = \mu_{{\rm H}*,i} - \mu_{*,i} - \mu_{{\rm H}'_{\rm (ag)}} - \mu_{\rm e}^{U_{\rm SHE}}$$
 (8)

for a site i. Substituting the equation (7) to the (8) results in

$$\Delta_{\rm r}G = \mu_{{\rm H}^*,i} - \mu_{*,i} - \frac{1}{2}\mu^{\circ}_{{\rm H}_{2({\rm g})}} + {\rm e}U_{\rm SHE} + \ln 10 \ k_{\rm B}T{\rm pH} \tag{9}$$

The first three terms are equivalent to the Gibbs free energy of hydrogen adsorption at site i,

$$\Delta_{\rm r}G_{{\rm ads},i} = \mu_{{\rm H}^*,i} - \mu_{*,i} - \frac{1}{2}\mu^{\rm o}_{{\rm H}_{2({\rm g})}} \tag{10}$$

Thus $\Delta_r G$ for the Volmer reaction is

Volmer:
$$\Delta_r G = \Delta_r G_{ads,i} + e U_{SHE} + \ln 10 \ k_B T p H$$
 (11)

Similarly, the previous steps can be applied to Heyrovsky reaction, $H_{(aq)}^+ + e^- + H^* \rightarrow H_{2(g)} + *$, resulting in:

Heyrovsky:
$$\Delta_{\rm r}G = -\Delta_{\rm r}G_{{\rm ads},i} + eU_{SHE} + \ln 10 \ k_BT$$
pH (12)

The Tafel reaction, $H^* + H^* \rightarrow H_{2(g)} + 2*$, does not involve proton and electron, and the electrode potential dependence is trivial,⁴ thus it is

Tafel:
$$\Delta_{\rm r}G = -\Delta_{\rm r}G_{{\rm ads},i} - \Delta_{\rm r}G_{{\rm ads},i}$$
 (13)

where $\Delta_r G_{ads,i}$ is the hydrogen adsorption energy for a site *i*. In the case of an alkaline reaction, using that the water dissociation, $H_2O_{(1)} \to H_{(aq)}^+ + OH_{(aq)}^-$, is fast and equilibrated simplifies the derivation.

$$\mu_{\rm H_2O_{(l)}} = \mu_{\rm H_{(aq)}^+} + \mu_{\rm OH_{(aq)}^-} \tag{14}$$

For example, the $\Delta_r G$ of the basic Volmer reaction, $H_2O_{(1)} + e^- + *\rightarrow H^* + OH_{(aq)}^-$, is:

$$\Delta_{\rm r}G = \Delta_{\rm r}G_{\rm ads} + \mu_{\rm OH_{(aq)}^-} - \mu_{\rm H_2O_{(l)}} - \mu_{\rm e^-}^{U_{\rm SHE}}$$
 (15)

Substituting the equation (14) to (15) results in (8), thus the $\Delta_r G$ for the acidic and basic Volmer reaction is the same, which is also the case for the Heyrovsky reaction. The diffusion between site is a non-electrochemical reaction thus the reaction energy is the difference in the adsorption energy:

Diffusion:
$$\Delta_{r}G = \Delta_{r}G_{ads,i} - \Delta_{r}G_{ads,i}$$
 (16)

where hydrogen atom diffuses from site j to site i. We note that the coverage effect – the interaction between the adsorbates – are included in the calculation $\Delta_{\rm r}G_{\rm ads}$ which we discuss in section 6.

1.3. Gibbs free energy of activation

The pH, electrode potential, and coverage effects manifest to the Gibbs free energy by affecting the energy of various states as summarized in Fig. S1 for Volmer reaction. Four states are considered for the acidic and basic condition: (1) $H_{(aq)}^+ + e^- + *$, (2) $H_{(HP)}^+ + e^- + *$ (3) transition state, and (4) H^* for acidic and, (1) $H_2O_{(1)} + e^- + *$, (2) transition state (3) $H^* + OH_{(HP)}^-$, and (4) $H^* + OH_{(aq)}^-$ for alkaline. $H_{(aq)}^+$ and $OH_{(aq)}^-$ represents the proton and $OH_{(HP)}^-$ in the bulk liquid as opposed to $H_{(HP)}^+$ and $OH_{(HP)}^-$ in the Helmholtz plane. Thus, the energetic difference between the (HP) and (aq) states represents the energy to shuttle the ion from the bulk liquid to the near-surface. Hence, $H_{(HP)}^+ + e^- + *$ represents the initial state that one would use to compute the barrier of proton transfer reaction using DFT and vice versa for $OH_{(HP)}^-$. Another point to note is that, for the acidic proton transfer, since the initial state represents proton in the non-bulk state, DFT calculated TS needs to be referenced from the final state (H*) as it only has water in the Helmholtz plane.

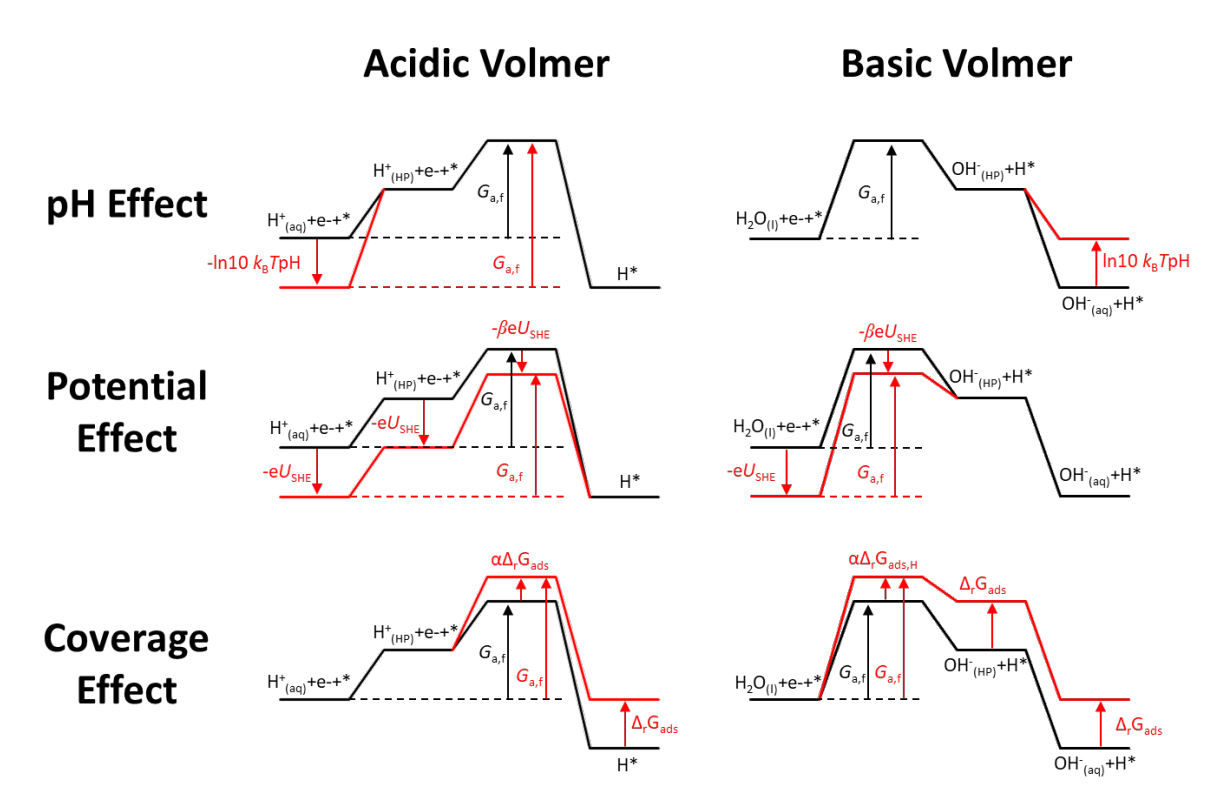


Fig. S1 | pH, potential, and coverage dependent reaction energetics for acidic and basic Volmer reaction. The same strategy can be applied to Heyrovsky reaction.

When the pH changes, only the chemical potential of $H_{(aq)}^+$ is affected, as it represents the bulk proton chemical potential. On the other hand, a proton in the Helmholtz plane $(H_{(HP)}^+)$ represents the particular, rarely observed configuration of water where the proton is near the surface, thus its chemical potential is not affected by the pH. Similarly, for basic reaction, only the chemical potential of $OH_{(aq)}^-$ is affected. As a result, only $G_{a,f}$, and $G_{a,r}$ are affected by pH for the reaction involving the proton transfer from hydronium, and water, respectively. Thus, $G_{a,f}(pH) = G_{a,f}^{\circ} + \ln 10 \ k_B T pH$ for acidic transfer and $G_{a,r}(pH) = G_{a,r}^{\circ} - \ln 10 \ k_B T pH$ for alkaline transfer.

For the change in the electrode potential, stable states involving electrons are shifted by $-eU_{\rm SHE}$. In the case of the transition state, energy is only shifted by the amount of the electron transfer involved in the transition state, which is the charge transfer coefficient, β . The energy of the transition state is shifted by $-\beta eU_{\rm SHE}$. Since the energy of the initial states also shifts for the proton transfer reactions, $G_{\rm a,f}(U_{\rm SHE}) = G^{\circ}_{\rm a,f} + (1-\beta)eU_{\rm SHE}$.

The change in reaction energy due to the coverage has been well-studied in the field. The increase in coverage increases the energy of H*, μ_{H*} , by laterally interacting with other adsorbates and ultimately increases $\Delta_r G_{ads}$ via equation (10). The change in the G_a are often described using Brønsted-Evans-Polanyi (BEP) relation: $G_{a,f} = \alpha \Delta_r G_{ads} + G^{\circ}_{a,f}$ for Volmer reaction, $G_{a,f} = \alpha(-\Delta_r G_{ads}) + G^{\circ}_{a,f}$ for Heyrovsky reaction, $G_{a,f} = \alpha(-\Delta_r G_{ads,i} - \Delta_r G_{ads,j}) + G^{\circ}_{a,f}$ for Tafel reaction, respectively. For Tafel reaction, i and j represent the two binding site involved in the Tafel reaction. We discuss in detail in section 6 below how lateral interaction dependent μ_{H*} is computed.

In summary, the $G_{a,f}$ are computed by:

Acidic reaction

Volmer:
$$G_{a,f} = \alpha(\Delta_r G_{ads,i}) + (1 - \beta)eU_{SHE} + \ln 10 k_B TpH + G_{a,f}^{\circ}$$

Heyrovsky:
$$G_{a,f} = \alpha(-\Delta_r G_{ads,i}) + (1 - \beta)eU_{SHE} + \ln 10 k_B T pH + G_{a,f}^{\circ}$$

Basic reaction

Volmer:
$$G_{a,f} = \alpha(\Delta_r G_{ads,i}) + (1 - \beta)eU_{SHE} + G_{a,f}^{\circ}$$
 (17)

Heyrovsky:
$$G_{a,f} = \alpha(-\Delta_r G_{ads,i}) + (1 - \beta)eU_{SHE} + G_{a,f}^{\circ}$$

Surface reaction

Tafel:
$$G_{a,f} = \alpha(-\Delta_r G_{ads,i} - \Delta_r G_{ads,j}) + G_{a,f}^{\circ}$$

Here, the $G^{\circ}_{a,f}$ is defined at $\Delta_r G_{ads} = U_{SHE} = pH = 0$. The parameters, α , β , and $G^{\circ}_{a,f}$ are retrieved from the previous works on the H/Pt system when possible (Table S1). We could not find α for the basic Volmer and Heyrovsky reaction so we develop the BEP relationship as discussed below. Also, β for the basic Volmer reaction is missing, which we assume is the same as the acidic Volmer reaction.

Table S1 | The parameters and their source for computing $G_{a,f}$ using the equation (2). The bold value in parenthesis indicates a model adjustment to reproduce experimental observation.

Reaction	α	β	<i>G</i> ° _{a,f}	α source	β source	$G^{\circ}_{a,f}$ source
Basic Volmer	0.881	0.44	1.270 (1.173)	This work	Ref ^{5a}	Ref ²
Basic Heyrovsky	0.511	0.59	1.360	This work	Ref^2	Ref ²
Tafel	0.462		0.514 (0.574)	Ref ^{5b}		Ref ^{5b}

^a β of acidic Volmer reaction from the reference used.

The diffusion-reaction is non-electrochemical and we use the diffusion BEP relationship universal for various adsorbates and elements⁶ where

$$G_{\rm af} = -0.13G_{\rm IS} - 0.11 \tag{18}$$

Here, G_{IS} represents the binding energy of hydrogen relative to its gaseous state:

^b Data sets for (111), (100), (110) are combined to calculate this parameter.

$$G_{\rm IS} = \mu_{\rm H*} - \mu_* - \mu^{\circ}_{\rm H_{(g)}} = \Delta_{\rm r} G_{{\rm ads},i} - \mu^{\circ}_{\rm H_{(g)}} + \frac{1}{2} \mu^{\circ}_{\rm H_{2(g)}}$$
(19)

This method only uses the initial state energy, thus the forward barrier calculated using the binding energy of the initial site and the reverse barrier calculated using the final site are not consistent (i.e. $E_{A,f} \neq E_{A,r} + \Delta_r E$). To ensure thermodynamic consistency, we use the average of the two barriers. We note that the averaging does not affect the result as diffusion reaction is not a rate determining step. Using $-\mu^{\circ}_{H(g)} + \frac{1}{2}\mu^{\circ}_{H_2(g)} = -2.27 \text{ eV}$, $G_{a,f}$ for hydrogen diffusion from site j to i is

Diffusion:
$$G_{a,f} = 0.435\Delta_r G_{ads,i} - 0.565\Delta_r G_{ads,i} + 0.184$$
 (20)

2. Density functional theory calculation details

In this work, we use density functional theory (DFT) for (1) computation of $\Delta_r G_{ads}$ to train prediction machine learning model, and (2) development of BEP relationship. Here we summarize the DFT parameter sets used. We perform DFT calculations using the Vienna Ab initio Simulation Package (VASP).⁷ Exchange and correlation energies are computed with the revised Perdew, Burke, and Ernzerhof (RPBE) functional,⁸ where the core electrons are treated with the projector augmented-wavefunction (PAW) method.^{9,10} We use a plane-wave basis set with a 400 eV kinetic energy cutoff for the valence electrons. The Brillouin zone is integrated using a $2\times2\times1$ Monkhorst-Pack k-mesh¹¹ for the machine learning data (cell size equivalent to 4×4 Pt(111) and Pt(100) slab), and $3\times3\times1$ Monkhorst-Pack k-mesh for the BEP relationship data ($c(4\times4)$ Pt(111) slab) with a Gaussian Methfessel-Paxton smearing of $0.1.^{12}$ The geometric optimization is performed until the residual force is less than 0.05 eV/Å.

For the calculation of the BEP relationship, the implicit solvation calculations are performed using the generalized Poisson-Boltzmann model as implemented in the VASPsol, 13,14 and the constant electrode potential (CEP) method. 15 The bulk relative permittivity of the water (78.4) is used. The Debye length is set to 3 Å, corresponding to a 1 M concentration of electrolyte (e.g. 1M KOH in our experiment). We add QV correction to address the spurious interaction between the finitely separated the slabs, where the Q and V are the net charges of the slab and the negative value of the electrostatic potential of bulk electrolyte, respectively. 16

3. Brønsted-Evans-Polanyi (BEP) relation development

To build a database for alkaline Volmer and Heyrovsky BEP relations, we employed a threelayer slab of $c(3\times4)$ with an optimized crystal lattice constant of 3.990 Å. To find the transition state (TS) structure, we used the nudged elastic band to obtain the TS structure¹⁷ which is refined at 0 V vs. SHE using the improved dimer method. 18 We considered Heyrovsky reaction at 0.08, 0.50, 1.00, 1.08, and 1.25 monolayer (ML), and for Volmer reaction at 0.00, 0.25, 0.42, 0.50, 0.58, 0.75, 0.83, 0.92, 1.00 and 1.25 ML. The established BEP relationship is shown in Fig. S2. Here, we only extracted the slope, α , for the $G_{a,f}$ calculation as shown in Table S1 for the reasons we describe below. The obtained slopes for basic Volmer (0.881) and Heyrovsky (0.511) are similar to those obtained for acidic Volmer (0.71) and Heyrovsky reactions (0.59).⁵ The slope for the basic Volmer reaction is also similar to the slope of the basic Volmer reaction (0.827) of Liu et al.¹⁹ A recent publication²⁰ discusses that the CEP method inconsistently describes the electrode potential due to multiple capacitances in the system, which can result in the deviation of $G^{\circ}_{a,f}$, (intercept). The $G_{a,f}$ obtained from Ref² using the constant charge method is 0.42 eV and 1.20 eV for Volmer and Heyrovsky at pH of 14, H* coverage of 0.00 ML and 0.08 ML in $c(3\times4)$ slab. At the same pH and H* coverage, we obtain 0.804 eV and 1.961 eV using the CEP method, respectively, which deviate significantly. Thus, we use the $G_{a,f}^{\circ}$ of the constant charge method by referencing to the $G_{a,f}$ at pH 14, and H* coverage of 0.00 ML and 0.08 ML.

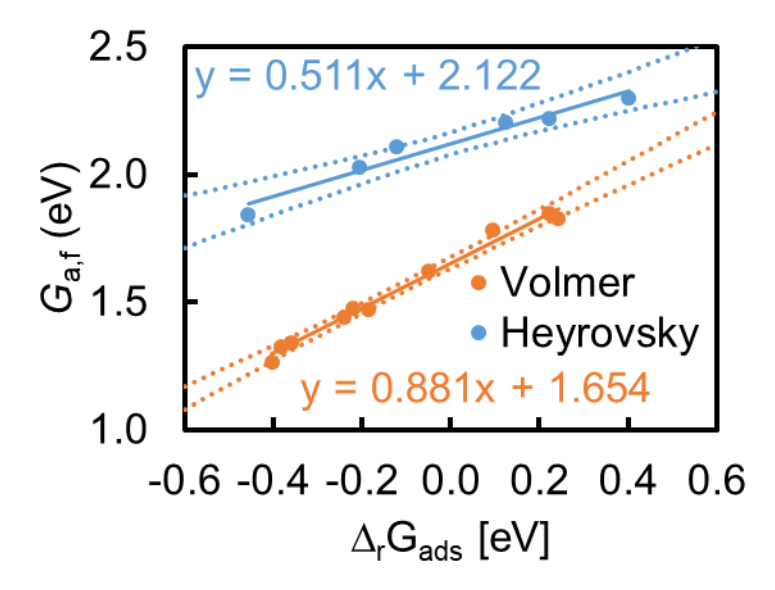


Fig. S2 | The coverage dependent alkaline BEP relationship for Volmer and Heyrovsky. The dotted line indicates the 95 confidence interval of the relations.

4. ReaxFF MD Simulation of the jagged Pt nanowire

To get a realistic structure of jagged Pt nanowire, we implement the force field based methods outlined in Ref²¹ which reproduces experimental characterization. Specifically

- 1. The infinite nanowire (1D system) is constructed based on the fcc Pt crystal structure where the z-axis of the nanowire is along the (111) direction. Along the x- and y-axis there are 13 and 9 Pt atoms. This choice was made to expose (100) facets.
- 2. The 1D model is replicated to 220 individual unit cells along the z-axis of the wire.
- 3. 85% of the Pt atoms are randomly selected and removed to simulate the Ni dealloying of 85:15 Ni:Pt nanowire.

- 4. The conjugate-gradient local relaxation is performed with a fixed-cell using the ReaxFF force field. The maximum change in Cartesian coordinates is limited to 0.1 Å to avoid disruption of the original structure. The nanowire is converged to 4×10^{-6} eV on the energy and 4×10^{-8} eV/Å on the force.
- 5. Another relaxation is performed with a relaxed cell along the z-direction at a pressure of 1 atm.
- 6. The NPT Molecular Dynamics (MD) simulation is performed at 343 K for 520 ps (20 ps equilibration followed by a 500 ps run).
- 7. The least coordinated atoms which would be leached away during ORR cycling are removed.
- 8. Another NPT Molecular Dynamics (MD) simulation is performed at 343 K for 520 ps (20 ps equilibration followed by a 500 ps run)
- 9. We relax the final structure using an EMT force field.²²
- Step 3 9 is applied to 4×4 Pt(111) and Pt(100) slabs to build a training set for the machine learning model where the number of slab layers is modified so the resulting slab would contain 64 Pt atoms.

5. Gibbs free energy of adsorption prediction via machine learning model development

As the jagged Pt nanowire surface is highly irregular and large, DFT is impractical to predict binding energy. Here, we leverage the machine learning model to make fast predictions on $\Delta_r \mu_{ads}$.

5.1. The Gibbs free energy of adsorption database

We sampled 200 structures for Pt(111) and Pt(100) each from the ReaxFF MD simulation protocol discussed above. We identified five to six binding sites, and their $\Delta_r G_{ads}$ were calculated using the DFT calculations (section 2), resulting in a total of 3413 data points. For geometric optimization, the Pt atom positions were fixed to preserve the geometry, while the H was allowed to move freely.

Our property of interest is $\Delta_r G_{ads} = \mu_{H*} - \mu_* - \frac{1}{2} \mu^{\circ}_{H_2(g)}$ as discussed above. Here, μ_* is the DFT calculated empty slab energy, $\mu^{\circ}_{H_2(g)}$ is the Gibbs free energy of the hydrogen gas at 1 bar where we account for the translational, rotational, and vibrational degree of freedom, and μ_{H*} is the Gibbs free energy of adsorbed hydrogen where the vibrational degree of freedom has been accounted for. For the vibrational contribution, we used the vibrational frequency obtained from Pt(111) hollow site for all 3413 calculations to reduce the computational cost.

5.2. Data preprocessing for machine learning model training

In this work, we tested the predictive accuracy of four different models: Atom centered symmetric function (ACSF), ²³ crystal graph convolutional neural networks (CGCNN), ²⁴ SchNet.²⁵ and Gaussian Process.²⁶ For the neural network model, we use the labeled site representation.²⁷ The labeled site is a simple representation involving labeling the binding site atoms. In this work, we label the binding site atoms by substituting the elements of the hydrogen interacting Pt with an element.²⁷ To find the binding site atoms, we use the alpha shape to identify top, bridge, and hollow binding sites and designate the binding site closest to the hydrogen as the hydrogen interacting binding site. The alpha shape is a shape formed by tetrahedral polygons of a set of points where a sphere of radius larger than a user-defined size cannot enter the polygons (See Ref²⁷ for the detailed explanation). By defining the sphere size as the sum of Van der Waals radius of hydrogen and platinum (2.84 Å), we can define the Pt surface where hydrogen gas would not be able to diffuse through without covalently interacting with the Pt surface. After the surface is defined, surface points, connection between points, and the center of the trigons of tetrahedral polygons become the top, bridge, and hollow site respectively. At this sphere size, the calculated electrochemical surface area (ECSA) is 106.8 m²/g comparable to the experimental ECSA of 112.9±5.4 m²/g²⁸ and 118 m²/g.²¹

To convert the DFT converged structures to machine (neural network) understandable representation, we focus on the local environment of the binding site similar to those introduced by Chen et al.²⁹ We used 7.0 Å from the binding site as a cutoff distance based on the first peak at 3.5 Å in the Pt-Pt radial distribution functions in jagged Pt nanowire to create machine learning representation. For the preparation of Gaussian process descriptors, we extracted the distance between the Pt atoms and the binding site for the 12 nearest Pt atoms. We designate this model as the nearest atom distance (NAD).

5.3. Model training and validation

In our previous work, we found that using the average of multiple models reduced model bias and improve the binding energy prediction accuracy, so-called ensemble modeling.²⁷ Here, we also use ensemble methods for predicting binding energy. To test our model, we hold out 10% of the dataset for testing and performed 5-fold CV using the rest of the data set (Fig. S3). Thus, we form five models for each method, and predictions are made to the 10% test set where the predictions are averaged before comparing with the true binding energies. As shown in Table S2, using the average prediction of five models shows higher accuracy than using one model alone. We also tested averaging the predictive accuracy of multiple model frameworks (e.g., ACSF and CGCNN), but the improvement was minimal. Here, we find that the ensemble of ACSF models shows the best performance with a mean absolute error of 0.043 eV, thus we use ACSF for predicting binding energies.

Test	Validation	Training			
10%	18%		72%		
10%		18%	72%		
10%			18%		
10%			72%	18%	
10%			72%		18%

Fig. S3 | Test, validation training split visualization for the 5-fold cross-validation used in this work.

Table S2 | Out-of-sample (test) set error statistics for various models considered. The red values indicate the lowest value within the columns. The plus sign indicates the combination of multiple machine learning methods. NAD is the Gaussian process method that uses the distance of Pt atoms nearest to the binding site as descriptors.

Model	Mean absolute error (eV)	Root mean squared error (eV)	Max absolute error (eV)
ASCF*	0.046	0.060	0.227
NAD*	0.057	0.073	0.283
CGCNN*	0.057	0.072	0.267
SchNet*	0.069	0.088	0.306
ASCF	0.043	0.056	0.221
NAD	0.057	0.073	0.287
CGCNN	0.056	0.071	0.243
SchNet	0.068	0.088	0.336
ASCF+NAD	0.046	0.059	0.211

ASCF+CGCNN	0.044	0.057	0.214
ASCF+SchNet	0.049	0.064	0.202
NAD+CGCNN	0.051	0.066	0.243
NAD+SchNet	0.057	0.074	0.279
CGCNN+SchNet	0.057	0.074	0.240
ASCF+NAD+CGCNN	0.046	0.059	0.207
ASCF+NAD+SchNet	0.049	0.063	0.231
ASCF+CGCNN+SchNet	0.049	0.063	0.201
NAD+CGCNN+SchNet	0.054	0.069	0.252
ASCF+NAD+CGCNN+SchNet	0.048	0.062	0.223

^{*}Best model out of five

5.4. Application to Jagged Pt Nanowire

To apply our model to the various Pt surfaces considered for KMC simulation, the alpha shape strategy discussed in section 5.2 is applied to the force field obtained Pt surfaces to find binding site atoms. Then, the site labeling and local environment pruning (see section 5.2.) are applied to predict binding energies.

6. Coverage effect model development

To apply the coverage effect introduced in Section 1, we need to model the lateral interaction, the repulsive interaction between the adsorbates. Here, we derive the hydrogen-hydrogen interaction energy from the experiments using the mean-field Ising (cluster expansion) model. We collected differential energy of adsorption for Pt(111), Pt(100), and Pt(110) from three different studies³⁰⁻³² and plotted it against the hydrogen surface density as shown in Fig. S4.

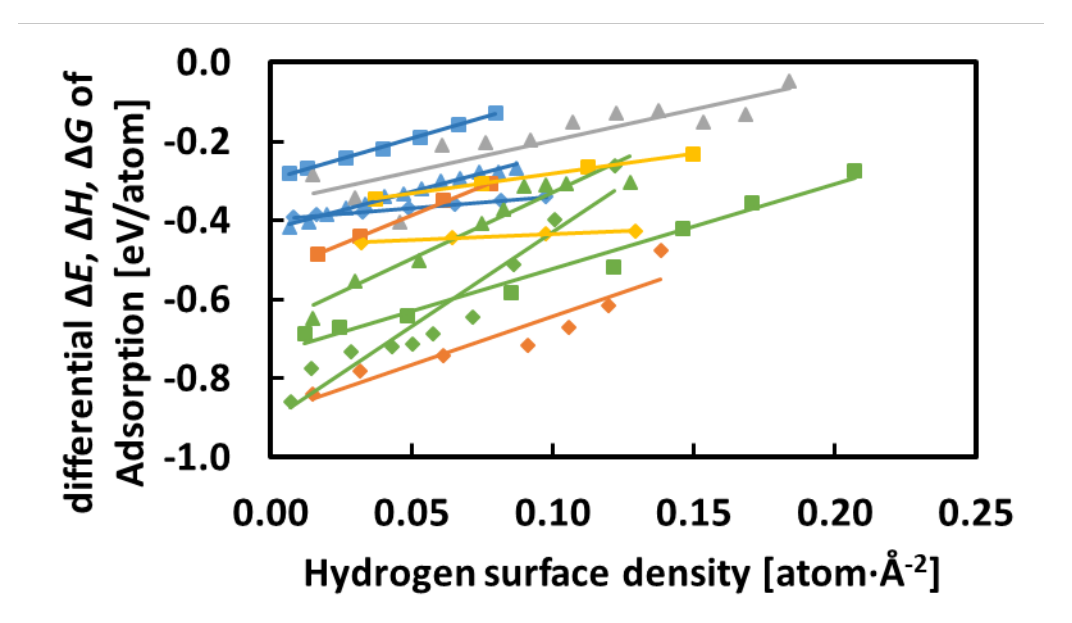


Fig. S4 | Differential energy, enthalpy, and Gibbs free energy of adsorption vs, the hydrogen surface for Pt(111) (Square), Pt(100) (diamond), and Pt(110) (triangle). Blue, gray, yellow, orange, and green colors from Ref, Ref, Ref, Ref, Ref, Ref, and Ref, 2 respectively. Y-axis value of Blue is Gibbs free energy (Δ G), those of gray and yellow are electronic energy (Δ E), and those of orange and green are enthalpy (Δ H) of adsorption.

Here, the change in adsorption energy (the slope in the figure) is fairly consistent between different surfaces and studies when plotted against the hydrogen surface density $(2.1 \pm 0.76 \, \text{eV} \cdot \text{Å}^2 \cdot \text{atom}^{-2})$, thus we use this information to estimate hydrogen-hydrogen lateral interaction. It has been shown that the nearest neighbor pair-wise interaction (Ising model) is sufficient to reproduce cyclo voltammetry data³⁴ thus we parameterize the Ising model using the experimental data.

Using the Ising model formulation, system energy can be written as

$$E = \sum_{i}^{N} E_{i} \sigma_{i} + J \sum_{\langle i, i \rangle}^{N} \sigma_{i} \sigma_{j}$$
 (21)

where E_i is the binding energy of site i, and σ_i is the occupancy where 0 is the unoccupied, and 1 is the occupied site, N is the number of sites. In the case of KMC simulation, equation (21) can be directly used as E_i and σ_i are rigorously calculated. We estimate J from

Fig. S4 by using mean-field theory to correlate to the experimental result. σ_i can be written as the fluctuation from its mean value, m_i

$$E = \sum_{i}^{N} E_{i} \sigma_{i} + J \sum_{\langle i,j \rangle}^{N} (m_{i} + d\sigma_{i}) (m_{i} + d\sigma_{j})$$
(22)

where $d\sigma_i = \sigma_i - m_i$, the fluctuation. Expanding the equation:

$$E = \sum_{i}^{N} E_{i} \sigma_{i} + J \sum_{\langle i,j \rangle}^{N} \left(m_{i} m_{j} + m_{i} d\sigma_{j} + m_{j} d\sigma_{i} + d\sigma_{i} d\sigma_{j} \right)$$
(23)

The last term is the product of two fluctuations, which is negligible at the limit of a large surface. Also, we assume that every site is equivalent in terms of lateral interaction for the simple parameterization (i.e., $m=m_i=m_j$). By accounting for these factors, and substituting the $d\sigma_i = \sigma_i - m_i$,

$$E = \sum_{i}^{N} E_{i} \sigma_{i} + J \sum_{\langle i,j \rangle}^{N} (m^{2} + 2m(\sigma_{i} - m))$$

$$= \sum_{i}^{N} E_{i} \sigma_{i} + J \sum_{\langle i,j \rangle}^{N} (-m^{2} + 2m\sigma_{i})$$
(24)

The summation over $\langle i,j \rangle$ can be written as $\sum_{\langle i,j \rangle}^{N} = 1/2 \sum_{i=1}^{N} \sum_{j \in nn(i)}^{N}$ where $\frac{1}{2}$ is to account for the double-counting, and nn(i) indicates the nearest-neighbor of i. Simplifying this expression result in:

$$E = \sum_{i}^{N} E_{i} \sigma_{i} - \frac{Jm^{2}Nz}{2} + Jmz \sum_{i}^{N} \sigma_{i}$$
 (25)

where N is the total number of sites, and z is the coordination number, i.e. the number of adjacent sites. This is the mean-field theory solution to the Ising model. Equation (25) represents the energy of the entire surface and

Fig. S4 is adsorption energy per site differentiated by hydrogen surface density $\rho_{\rm H} = \frac{N_{\rm H}}{N} \rho_{\rm S}$, where $N_{\rm H} = \sum_i^{\rm N} \sigma_i$ is the number of hydrogen, and $\rho_{\rm S}$ is the surface site density. Dividing the Equation (25) by $N_{\rm S}$ to get energy per site and using that $m = \frac{N_{\rm S}}{N}$, and E_i is consistent for single facet (= E_0), Equation (25) simplifies to:

$$\frac{E}{N_{\rm H}} = E_0 + \frac{Jz}{2} \frac{\rho_{\rm H}}{\rho_{\rm S}} \tag{26}$$

Taking the first derivative results in the slope of

Fig. S4:

$$\frac{dE/N_{\rm H}}{d\rho_{\rm H}} = \frac{Jz}{2\rho_{\rm S}} \tag{27}$$

Here, we use ρ_S equal to 0.14 atom/Å², the average of 0.15, 0.13, and 0.14 atom/Å² for (111), (100), and (110) – (1×2) respectively. In all three surfaces, z is 6, by considering only the sites that are filled by hydrogen before the over-saturation (>1 ML), resulting in J = 0.098 ± 0.035 eV. The sites on nanowire may have more than 6 nearest neighbor sites thus local oversaturation is plausible, but the oversaturation is not observed until very low potential which is not considered in this study. The distances between sites in single crystal surfaces are all within 2.78 Å, thus, for nanowire, sites within 2.78 Å radius are identified for each site and are considered nearest-neighbors for lateral interactions.

To apply this model to our system, μ_{H*} can be further expanded:

$$\mu_{H*} = \mu^{\circ}_{H*} + J\Delta n_{H-H} \tag{28}$$

where μ°_{H*} indicates the energy of adsorbed hydrogen at the zero-coverage limit, Δn_{H-H} is the change in the number of H-H interactions (number of hydrogen pairs are within 2.78 Å) between the final and initial states. The zero-coverage limit is the coverage where lowering the coverage no-longer changes the adsorption energy. For the Gibbs free energy of adsorption database we have built, the hydrogen atoms are sufficiently far apart across the periodic boundary that the lateral interaction is not felt across the periodic boundary. For the KMC simulation, graph theory can be used to compute Δn_{H-H} .

7. Graphic theoretical kinetic Monte Carlo simulation

The graphic theoretical kinetic Monte Carlo provides site-resolved insights into catalysis that are otherwise not possible using the mean-field microkinetic models and experiments. In this method, each binding site is explicitly defined and a reaction is simulated one at a time, thus provides a high-resolution picture into catalysis as shown in Fig. S5 with a Pt(111) example. A great review is provided in ref.³⁵ In this section, we summarize the methodology for Pt surface graph generation, the graphical definition of reactions, the Kinetic Monte Carlo algorithm, and the model validation and adjustments.

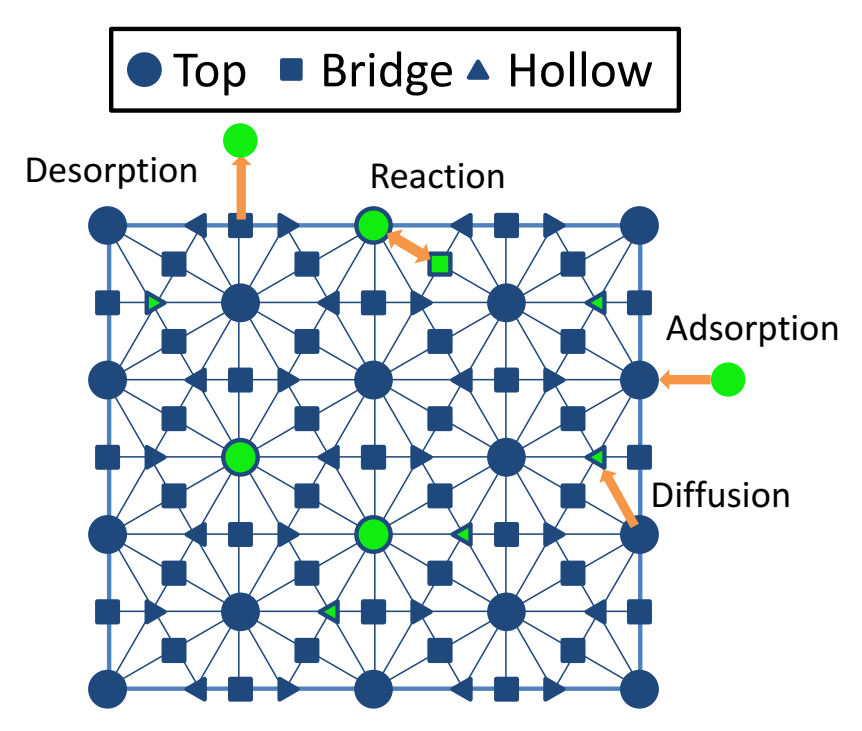


Fig. S5 | An Pt(111) example of a graph theoretical kinetic Monte Carlo. The green and blue fill represents the adsorbate and the empty binding sites. In graphical kinetic Monte Carlo reactions are simulated one at a time with the site-resolved picture to provide catalytic insights.

7.1. Pt surface graph generation, and reaction graph definition

To generate the surface graph, we use the alpha shape procedure introduced in section 5.2. From the ReaxFF, we sampled the jagged Pt nanowire's structure, and alpha shape is used to convert its surface the polygonal shape, where the points are the atoms/top sites, the edges of the polygons are the bridge site and the center of the triangle is the hollow site. The Volmer and Heyrovsky reactions are available to all sites, whereas Tafel and diffusion reactions are defined for a pair of adjacent sites as shown in Fig. S6.

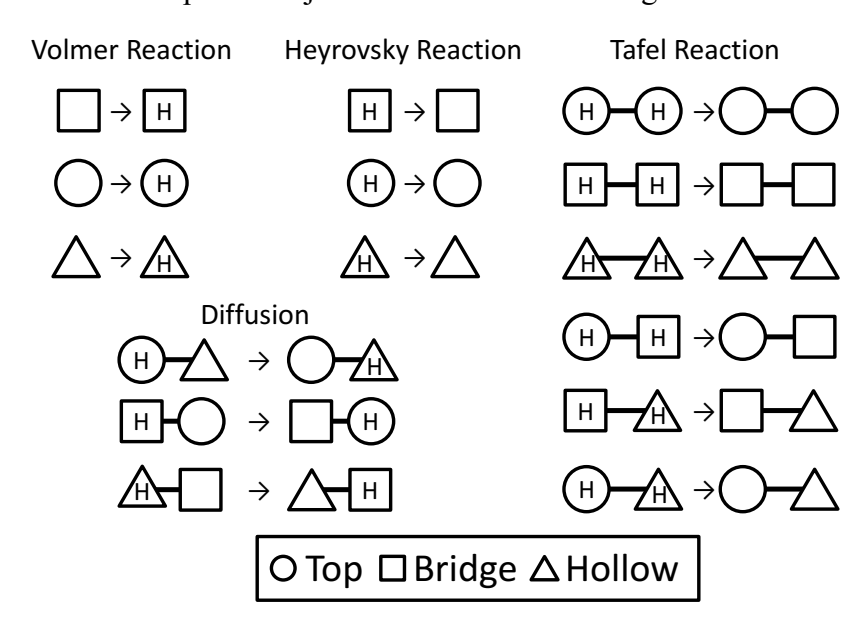


Fig. S6 | The change in the surface graph for each reaction type.

7.2. Kinetic Monte Carlo algorithm

We used the graph-theoretical kinetic Monte Carlo algorithm as outlined in Stamatakis et al³⁵ and we also implemented the reaction scaling method by Núñez et al³⁶ to speed up the simulation. Reaction constants are calculated using the transition state theory and thermodynamic equilibrium:

$$k_{\rm f} = \frac{k_{\rm b}T}{h} \exp\left(\frac{-G_{\rm a,f}}{k_{\rm b}T}\right)$$

$$k_{\rm r} = \frac{k_{\rm f}}{K}$$

$$K = \exp\left(\frac{-\Delta_{\rm r}G}{k_{\rm b}T}\right)$$
(29)

The pseudo-code for the KMC algorithm is provided below:

- 0. Start
- 1. Initialize all reaction constants
- 2. Run parallel KMC simulations until 1000 events
- 3. Rescale the fast equilibrated reactions as described in Ref³⁶
- 4. Set the termination time for the next run to be twice the first run
- 5. Run parallel KMC simulation until the termination time
- 6. Rescale the fast equilibrated reactions
- 7. Repeat 4-6 until the system reaches the steady-state (which we define as when the noise in the current density is within $\sim 10\%$)

We used the rejection-free KMC algorithm as it is the fastest algorithm for our system.

7.3. Model validation, degree of rate control analysis, uncertainty, and adjustments

The followings are the supplementary figures and tables regarding the model validation.

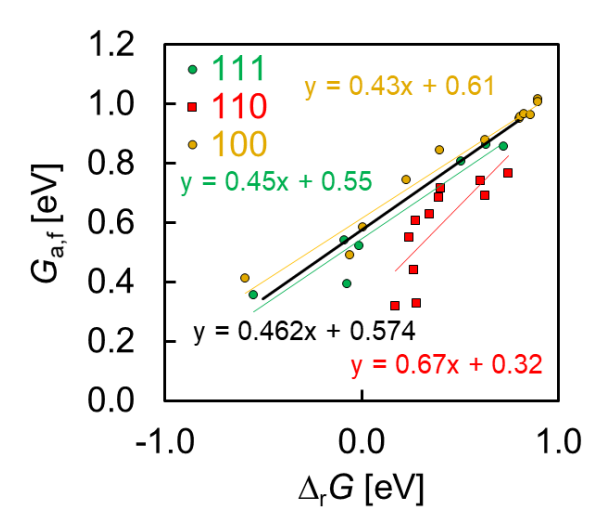


Fig. S7 | Tafel reaction BEP trends obtained from ref⁵ for Pt(111) (green), Pt(110) (red), and Pt(100) (Yellow). In our model, we use the black trend line which falls well within the distribution of the data.

Table S3 | Higher and lower bounds of reproduced measurements based on 95% confidence intervals of sensitive parameters. BV and M indicate Butler-Volmer and micropolarization fitting, respectively.

	Lateral Interaction (<i>J</i>)	Tafel BEP relation	Volmer BEP relation
Tafel Slope (mV/dec)	72.9 (72.5, 77.5)	72.9 (71.1, 85.7)	72.9 (72.1, 75.5)
BV i_0 (mA cm ⁻²)	0.81 (0.60, 1.12)	0.81 (0.62, 0.83)	0.81 (0.36, 1.72)
$BV\beta$	0.46 (0.45, 0.48)	0.46 (0.45, 0.52)	0.46 (0.46, 0.47)
$M i_0 (mA cm^{-2})$	0.83 (0.60, 1.12)	0.83 (0.63, 0.85)	0.83 (0.40, 1.72)
Bifunctional Gain	4.61 (3.10, 4.81)	4.61 (2.78, 6.12)	4.61 (3.02, 4.67)

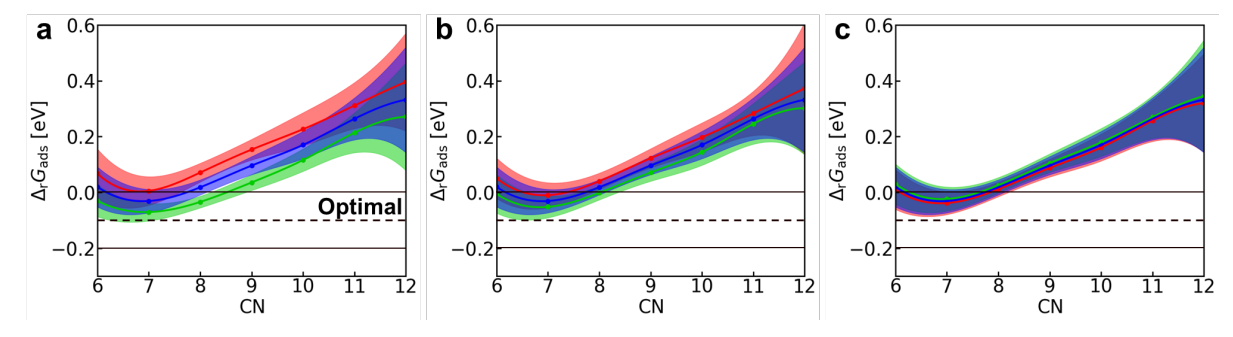


Fig. S8 | Change in $\Delta_r G_{ads}$ vs. CN within the 95 confidence interval of (a) J (HH cluster interaction energy) (b) Tafel barriers and (c) Volmer barriers. The blue, red, and green colors indicate the norm, upper, and lower interval. Overall the conclusion that Pt atom with lower CN is the active centers remains the same.

7.4. Effect of jagged Pt nanowire length

We made 46.1 nm nanowire using the force field approach, and we cut the wire at various lengths to produce the Figures in this study. To check the validity using a shorter wire, we plot the zero coverage Gibbs free energy of adsorption, $\Delta_r G_{\rm ads,0}$, at various lengths, as shown in Fig. S9. The larger wire length results in a smoother normal distribution. We test the normality of the distribution using a 2-sided chi-squared probability for skewness and kurtosis, which is all below 0.296% of 2.3 nm signifying their normality (Table S4). We find that the current density is within 10% of each other for all tested lengths (2.3, 4.6, 9.2, and 23.0 nm) of the wire

(Table S4). At the minimum, we used a 2.3 nm wire length to produce results that are sufficient to reproduce the macroscopic behavior.

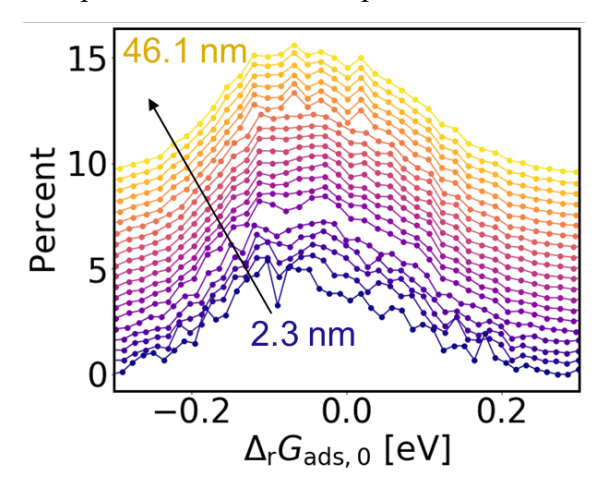


Fig. S9 | The distribution of zero coverage Gibbs free energy of adsorption, $\Delta_{\rm r}G_{\rm ads,0}$, for various length of the jagged Pt nanowire (with an offset of 0.5 for each increase in length)

Table S4 | A 2-sided chi-squared probability for normality (skewness and kurtosis test) for zero coverage Gibbs free energy of adsorption, $\Delta_{\rm r}G_{\rm ads,0}$ of jagged Pt nanowire at various length, L at pH 14, 298K and -0.05 V vs. RHE and 1 bar H₂

	$\Delta_{\rm r}G_{\rm ads,0}$	Steady State	Output Figures and Tables
L (nm)	normality X ²	<i>i</i> (mA cm ⁻²)	
2.3	2.96×10 ⁻³	1.76 ± 0.08	Fig. 2, Table S3, Fig. S8
4.6	2.28×10 ⁻⁴	1.71 ± 0.02	Fig. 4
6.9	3.18×10 ⁻⁴		
9.2	2.08×10 ⁻⁵	1.75 ± 0.02	Fig. 3bc, Fig. 6
11.5	6.01×10 ⁻⁸		
13.8	8.64×10 ⁻⁸		
16.1	5.54×10 ⁻⁹		
18.4	2.76×10 ⁻⁹		
20.7	5.14×10 ⁻¹¹		
23.0	2.64×10 ⁻¹²	1.96 ± 0.02	Fig. 3a, Fig. 7, Fig. S10
25.4	3.52×10 ⁻¹⁴		
27.7	2.84×10 ⁻¹⁵		
30.0	2.53×10 ⁻¹⁸		
32.3	1.39×10 ⁻¹⁹		
34.6	4.84×10 ⁻¹⁹		
36.9	9.56×10 ⁻²³		
39.2	3.24×10 ⁻²⁴		
41.5	4.19×10 ⁻²⁶		
43.8	2.28×10 ⁻²⁸		
46.1	7.84×10 ⁻²⁶		

8. Experimental details

8.1. Synthesis of PtNi alloy nanowire on carbon

All chemicals were purchased from Sigma-Aldrich unless otherwise specified. In a typical synthesis, 20 mg Pt(acac)₂ and 40 mg Ni(acac)₂ were mixed with 130 mg glucose, 1.7 mg W(CO)₆ and 60 mg PVP (molecular weight: 40000) in a glass vial, with 3 ml of oleylamine and 2 mL octadecene as co-solvent. The mixture was heated to 140 °C for 6 h to form Pt–NiO core–shell nanowires. The resulting nanowires were collected via centrifuge at 7,000 r.p.m. for 20 min. After loading the nanowires on pretreated Vulcan 72 carbon black, the catalysts were then annealed under 450 °C in argon/hydrogen (97:3) atmosphere for 12 h to obtain the PtNi alloy nanowires supported on carbon black.

8.2. Electrochemical dealloying of PtNi nanowire to synthesize jagged Pt nanowire

The ink was prepared by dispersing 1 mg catalysts and 10 uL Nafion solution in 1 mL ethanol using sonication. 10 uL ink was then dropcasted on the rotating disk electrode (RDE: 0.196 cm²) as the working electrode. The Ag/AgCl electrode and the Pt wire were used as the reference electrode and the counter electrode, respectively. The potential of the reference electrode has been pre-calibrated under 1 atmosphere H₂. An electrochemical dealloying process was performed via 200 cyclic voltammetry (CV) cycles of working electrode between 0.05 V and 1.10 V versus RHE in 0.1 M HClO₄ at a scan rate of 100 mV/s to completely remove the nickel species. N₂ gas was continuously purged to remove the O₂ from the electrolyte. After complete dealloying, the remained Pt surface then became a jagged surface which has been characterized by previous works.

8.3. Electrochemical hydrogen evolution/oxidation reaction test

After dealloying, the working electrode was carefully washed using deionized water and transferred into 1 M KOH electrolyte (N_2) purge and scan CV from 0.05 V to 1.10 V vs. RHE at a scan rate of 100 mV/s until the CV is stable. The reference electrolyte and counter electrode used in 1 M KOH were Hg/HgO electrode and graphite rod electrode, respectively. The HER/HOR tests were then performed via linear scan voltammetry (LSV) from -0.05 V to 0.10 V vs. RHE at a scan rate of 10 mV/s with continuous H_2 purging. All the presented HER/HOR polarization curves and following data analysis are iR-corrected.

8.4. Obtaining exchange current density, symmetric factor, and Tafel slope from the HER/HOR Polarization curve

After obtaining the HER/HOR polarization curve, the HOR branch was corrected by Koutecky–Levich equation (eq. (30)), where j is the current density collected on the working electrode and j_k is the kinetic current density and j_d is the H₂-diffusion limiting current density. The corrected HER/HOR polarization curve was then fitted from -0.05 V to 0.05 V using Butler–Volmer equation (eq. (31)), and fitted from -0.01 V to 0.01 V using micropolarization linear fitting (eq. (32)), to get symmetric factor β and the exchange current density $j_{\theta, RDE}$ (normalized by RDE geometric surface area). Here, R is the universal gas constant, T is the temperature in Kelvin, F is the Faraday's constant, and η is the overpotential. The Tafel slope was then directly measured from the Butler–Volmer plot.

$$\frac{1}{j} = \frac{1}{j_k} + \frac{1}{j_d} \tag{30}$$

$$j_k = j_{0,RDE} \times \left(e^{\frac{\beta F \eta}{RT}} - e^{\frac{(\beta - 1)F \eta}{RT}}\right)$$
(31)

$$j = j_{0,RDE} \times \frac{\eta F}{RT} \tag{32}$$

After obtaining $j_{0, RDE}$, the intrinsic exchange current density $i_{0, ECSA}$ was determined by the following simple calculation (33). Here the A_{Hupd} is the hydrogen underpotential deposition area of the jagged Pt nanowires, which was determined from its CV plot in 1 M KOH.

$$i_0 = j_{0,RDE} \frac{0.196}{A_{Hupd}} \tag{33}$$

9. Supplementary Figures and Tables

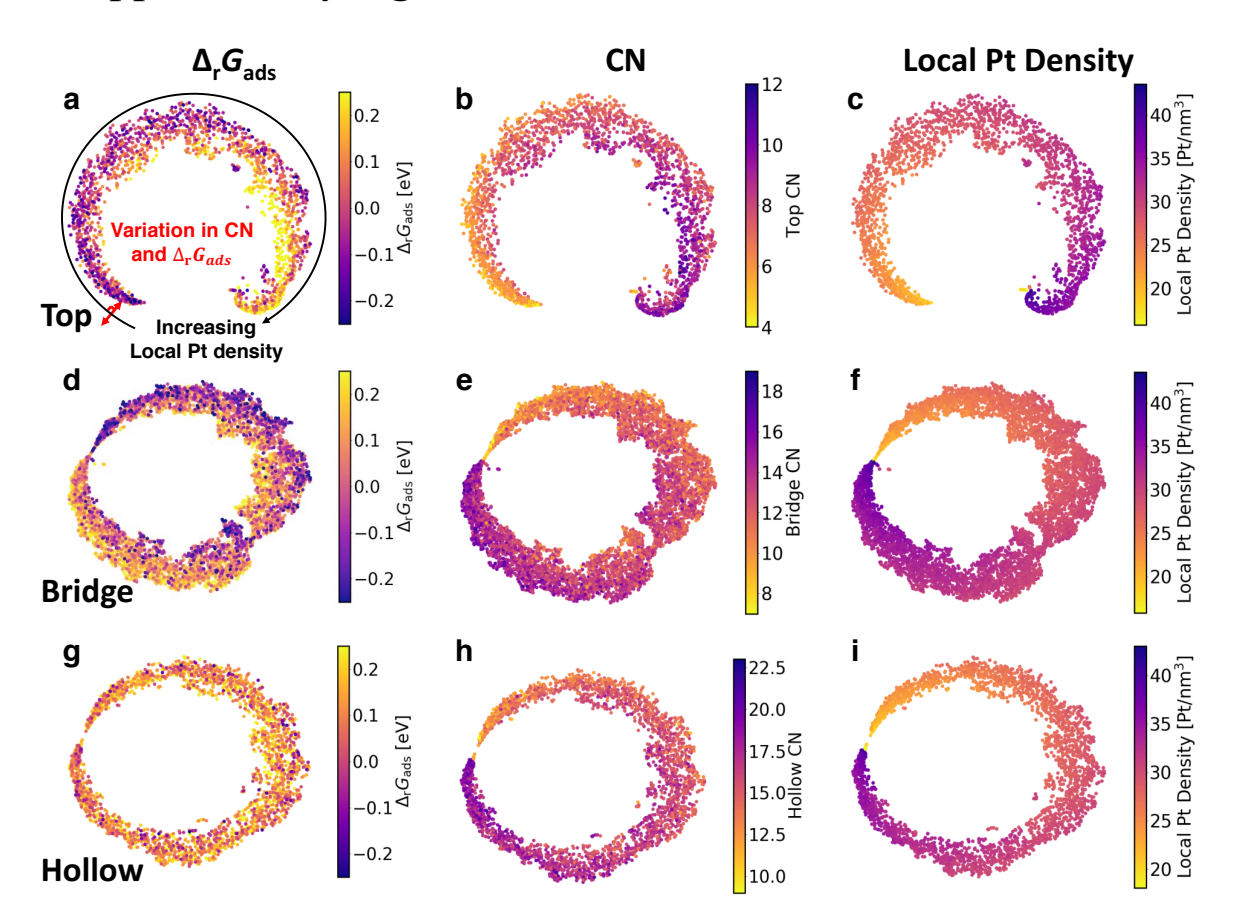


Fig. S10 | Visualization of the optimized latent coordinate of sites based on the similarity between sites for each site type: top (\mathbf{a} , \mathbf{b} , \mathbf{c}), bridge (\mathbf{d} , \mathbf{e} , \mathbf{f}), and hollow sites (\mathbf{g} , \mathbf{h} , \mathbf{i}). The colors represent $\Delta_r G_{ads}$ (\mathbf{a} , \mathbf{d} , \mathbf{g}), coordination number (CN) (\mathbf{b} , \mathbf{e} , \mathbf{h}), and local Pt density (\mathbf{c} , \mathbf{f} , \mathbf{i}). The t-SNE optimized sites' latent coordinates based on the CN and the local Pt density. The examination shows that CN is correlated to the $\Delta_r G_{ads}$.

10. Reference

- (1) Lindgren, P.; Kastlunger, G.; Peterson, A. A. A Challenge to the $G \sim 0$ Interpretation of Hydrogen Evolution. *ACS Catal.* **2020**, *10*, 121.
- (2) Lamoureux, P. S.; Singh, A. R.; Chan, K. pH Effects on Hydrogen Evolution and Oxidation over Pt(111): Insights from First-Principles. *ACS Catal.* **2019**, *9*, 6194.
- (3) Nørskov, J. K.; Rossmeisl, J.; Logadottir, A.; Lindqvist, L.; Kitchin, J. R.; Bligaard, T.; Jónsson, H. Origin of the Overpotential for Oxygen Reduction at a Fuel-Cell Cathode. *J. Phys. Chem. B* **2004**, *108*, 17886.
- (4) Fang, Y.-H.; Wei, G.-F.; Liu, Z.-P. Catalytic Role of Minority Species and Minority Sites for Electrochemical Hydrogen Evolution on Metals: Surface Charging, Coverage, and Tafel Kinetics. *J. Phys. Chem. C* **2013**, *117*, 7669.
- (5) Skúlason, E.; Tripkovic, V.; Björketun, M. E.; Gudmundsdóttir, S.; Karlberg, G.; Rossmeisl, J.; Bligaard, T.; Jónsson, H.; Nørskov, J. K. Modeling the Electrochemical Hydrogen Oxidation and Evolution Reactions on the Basis of Density Functional Theory Calculations. *J. Phys. Chem. C* **2010**, *114*, 18182.
- (6) Peng, G.; Mavrikakis, M. Adsorbate Diffusion on Transition Metal Nanoparticles. *Nano Lett.* **2015**, *15*, 629.
- (7) Kresse, G.; Furthmüller, J. Efficient iterative schemes for *ab initio* total-energy calculations using a plane-wave basis set. *Phys. Rev. B* **1996**, *54*, 11169.
- (8) Hammer, B.; Hansen, L. B.; Nørskov, J. K. Improved adsorption energetics within density-functional theory using revised Perdew-Burke-Ernzerhof functionals. *Phys. Rev. B* **1999**, *59*, 7413.
- (9) Blöchl, P. E. Projector augmented-wave method. *Phys. Rev. B* **1994**, *50*, 17953.
- (10) Kresse, G.; Joubert, D. From ultrasoft pseudopotentials to the projector augmented-wave method. *Phys. Rev. B* **1999**, *59*, 1758.
- (11) Monkhorst, H. J.; Pack, J. D. Special points for Brillouin-zone integrations. *Phys. Rev. B* **1976**, *13*, 5188.
- (12) Methfessel, M.; Paxton, A. T. High-precision sampling for Brillouin-zone integration in metals. *Phys. Rev. B* **1989**, *40*, 3616.
- (13) Mathew, K.; Kolluru, V. C.; Mula, S.; Steinmann, S. N.; Hennig, R. G. Implicit self-consistent electrolyte model in plane-wave density-functional theory. *J. Chem. Phys.* **2019**, *151*, 234101.
- (14) Mathew, K.; Sundararaman, R.; Letchworth-Weaver, K.; Arias, T.; Hennig, R. G. Implicit solvation model for density-functional study of nanocrystal surfaces and reaction pathways. *J. Chem. Phys.* **2014**, *140*, 084106.
- (15) Van den Bossche, M.; Skúlason, E.; Rose-Petruck, C.; Jónsson, H. Assessment of Constant-Potential Implicit Solvation Calculations of Electrochemical Energy Barriers for H2 Evolution on Pt. *J. Phys. Chem. C* **2019**, *123*, 4116.
- (16) Van den Bossche, M.; Skúlason, E.; Rose-Petruck, C.; Jónsson, H. Addition to "Assessment of Constant-Potential Implicit Solvation Calculations of Electrochemical Energy Barriers for H2 Evolution on Pt". *J. Phys. Chem. C* **2019**, *123*, 15875.
- (17) Henkelman, G.; Jónsson, H. Improved tangent estimate in the nudged elastic band method for finding minimum energy paths and saddle points. *J. Chem. Phys.* **2000**, *113*, 9978.
- (18) Heyden, A.; Bell, A. T.; Keil, F. J. Efficient methods for finding transition states in chemical reactions: Comparison of improved dimer method and partitioned rational function optimization method. *J. Chem. Phys.* **2005**, *123*, 224101.

- (19) Liu, L.; Liu, Y.; Liu, C. Enhancing the Understanding of Hydrogen Evolution and Oxidation Reactions on Pt(111) through Ab Initio Simulation of Electrode/Electrolyte Kinetics. *J. Am. Chem. Soc.* **2020**, *142*, 4985.
- (20) Gauthier, J. A.; Dickens, C. F.; Heenen, H. H.; Vijay, S.; Ringe, S.; Chan, K. Unified Approach to Implicit and Explicit Solvent Simulations of Electrochemical Reaction Energetics. *J. Chem. Theory Comput.* **2019**, *15*, 6895.
- (21) Li, M.; Zhao, Z.; Cheng, T.; Fortunelli, A.; Chen, C.-Y.; Yu, R.; Zhang, Q.; Gu, L.; Merinov, B. V.; Lin, Z.; Zhu, E.; Yu, T.; Jia, Q.; Guo, J.; Zhang, L.; Goddard, W. A.; Huang, Y.; Duan, X. Ultrafine jagged platinum nanowires enable ultrahigh mass activity for the oxygen reduction reaction. *Science* **2016**, *354*, 1414.
- (22) Jacobsen, K. W.; Stoltze, P.; Nørskov, J. K. A semi-empirical effective medium theory for metals and alloys. *Surf Sci.* **1996**, *366*, 394.
- (23) Behler, J. Atom-centered symmetry functions for constructing high-dimensional neural network potentials. *J. Chem. Phys.* **2011**, *134*, 074106.
- (24) Xie, T.; Grossman, J. C. Crystal Graph Convolutional Neural Networks for an Accurate and Interpretable Prediction of Material Properties. *Phys. Rev. Lett.* **2018**, *120*, 145301.
- (25) Schütt, K. T.; Sauceda, H. E.; Kindermans, P. J.; Tkatchenko, A.; Müller, K. R. SchNet A deep learning architecture for molecules and materials. *J. Chem. Phys.* **2018**, *148*, 241722.
- (26) Rasmussen, C. E. In *Advanced Lectures on Machine Learning: ML Summer Schools 2003, Canberra, Australia, February 2 14, 2003, Tübingen, Germany, August 4 16, 2003, Revised Lectures*; Bousquet, O., von Luxburg, U., Rätsch, G., Eds.; Springer Berlin Heidelberg: Berlin, Heidelberg, 2004, p 63.
- (27) Gu, G. H.; Noh, J.; Kim, S.; Back, S.; Ulissi, Z.; Jung, Y. Labeled Site Representation for Ensemble Deep-Learning of Binding Energy Prediction for Accurate Heterogeneous Catalyst Screening. *J. Phys. Chem. Lett.* **2020**, (submitted).
- (28) Li, M.; Duanmu, K.; Wan, C.; Cheng, T.; Zhang, L.; Dai, S.; Chen, W.; Zhao, Z.; Li, P.; Fei, H.; Zhu, Y.; Yu, R.; Luo, J.; Zang, K.; Lin, Z.; Ding, M.; Huang, J.; Sun, H.; Guo, J.; Pan, X.; Goddard, W. A.; Sautet, P.; Huang, Y.; Duan, X. Single-atom tailoring of platinum nanocatalysts for high-performance multifunctional electrocatalysis. *Nat. Catal.* **2019**, *2*, 495.
- (29) Chen, Y.; Huang, Y.; Cheng, T.; Goddard, W. A. Identifying Active Sites for CO2 Reduction on Dealloyed Gold Surfaces by Combining Machine Learning with Multiscale Simulations. *J. Am. Chem. Soc.* **2019**, *141*, 11651.
- (30) Gómez, R.; Orts, J. M.; Álvarez-Ruiz, B.; Feliu, J. M. Effect of Temperature on Hydrogen Adsorption on Pt(111), Pt(110), and Pt(100) Electrodes in 0.1 M HClO4. *J. Phys. Chem. B* **2004**, *108*, 228.
- (31) Ross, P. N. Hydrogen chemisorption on Pt single crystal surfaces in acidic solutions. *Surface Science* **1981**, *102*, 463.
- (32) Will, F. G. Hydrogen Adsorption on Platinum Single Crystal Electrodes. *J. Electrochem. Soc.* **1965**, *112*, 451.
- (33) Gudmundsdóttir, S.; Skúlason, E.; Weststrate, K.-J.; Juurlink, L.; Jónsson, H. Hydrogen adsorption and desorption at the Pt(110)-(1×2) surface: experimental and theoretical study. *PCCP* **2013**, *15*, 6323.
- (34) Karlberg, G. S.; Jaramillo, T. F.; Skúlason, E.; Rossmeisl, J.; Bligaard, T.; Nørskov, J. K. Cyclic Voltammograms for H on Pt(111) and Pt(100) from First Principles. *Phys. Rev. Lett.* **2007**, *99*, 126101.
- (35) Stamatakis, M.; Vlachos, D. G. A graph-theoretical kinetic Monte Carlo framework for onlattice chemical kinetics. *J. Chem. Phys.* **2011**, *134*, 214115.

(36) Núñez, M.; Robie, T.; Vlachos, D. G. Acceleration and sensitivity analysis of lattice kinetic Monte Carlo simulations using parallel processing and rate constant rescaling. *J. Chem. Phys.* **2017**, *147*, 164103.